Heteroepitaxy of Ge on singular and vicinal Si surfaces: elastic field symmetry and nanostructure growth

2015 J. Phys.: Condens. Matter 27 253001

(http://iopscience.iop.org/0953-8984/27/25/253001)

IOP Publishing Journal of Physics: Condensed Matter
J. Phys.: Condens. Matter **27** (2015) 253001 (28pp) doi:10.1088/0953-8984/27/25/253001

Topical Review

Heteroepitaxy of Ge on singular and vicinal Si surfaces: elastic field symmetry and nanostructure growth

L Persichetti[1], A Sgarlata[2], M Fanfoni[2] and A Balzarotti[2]

[1] Department of Materials, ETH Zurich, Hönggerbergring 64, CH - 8093 Zürich, Switzerland
[2] Dipartimento di Fisica, Università di Roma 'Tor Vergata', Via della Ricerca Scientifica 1, 0133 Roma, Italy

E-mail: sgarlata@roma2.infn.it

Received 21 October 2014, revised 20 February 2015
Accepted for publication 8 April 2015
Published 28 May 2015

Abstract
Starting with the basic definition, a short description of a few relevant physical quantities playing a role in the growth process of heteroepitaxial strained systems, is provided. As such, the paper is not meant to be a comprehensive survey but to present a connection between the Stranski–Krastanov mechanism of nanostructure formation and the basic principles of nucleation and growth. The elastic field is described in the context of continuum elasticity theory, using either analytical models or numerical simulations. The results are compared with selected experimental results obtained on GeSi nanostructures. In particular, by tuning the value of quantities such as vicinality, substrate orientation and symmetry of the diffusion field, we elucidate how anisotropic elastic interactions determine shape, size, lateral distribution and composition of quantum dots.

Keywords: nucleation, vicinal surfaces, SiGe, heteroepitaxial growth, nanostructures

(Some figures may appear in colour only in the online journal)

1. Introduction

More than twenty years have passed since the early works of Mo *et al* [1] and Eaglesham and Cerullo [2] demonstrated the formation of *coherent* nanoscale islands (nanocrystals (NCs) or quantum dots (QDs)) during the epitaxial growth of suitable lattice-mismatched semiconductor pairs. Thenceforth, intensive efforts have been devoted to the Stranski–Krastanov's (SK) growth of Ge on Si surfaces. The interest in Ge/Si epitaxy stems from two interconnected sources. On the one hand, this system has a great deal of potential in technological applications compatible with standard Si technology, such as quantum computing and quantum information devices [3, 4]. On the other hand, it has been recognized as an ideal prototype system for modeling the fascinating and complex phenomena related to strained heteroepitaxy and for investigating the properties of QDs' spontaneous formation. The possibility of developing simple yet predictive models for epitaxial growth has driven a huge amount of literature on Ge/Si, including many excellent monographs and review papers surveying the different aspects of the subject [5–8]. In this context, our purpose is to look at the Ge/Si epitaxy from a peculiar and, hopefully, original perspective: we have not followed the usual 'historical' approach of surveying all the various contributions to the subject present in the literature. Rather we have chosen a few selected cases which drive the growth of Ge/Si nanostructures and have gone on to elucidate the connection between the elastic field and symmetry, shaping, faceting and composition. To this end our review includes some unpublished material by the authors such as independent calculations or measurements as well as adaptations of original data and figures.

The paper is organized as follows: after briefly reviewing some basic concepts of elasticity theory, we focus on how a

realistic three-dimensional (3D) modeling of the elastic field in epitaxial nanostructures can be obtained by finite-element (FE) simulations. In particular, we highlight the link between island shape and elastic field symmetry. Then, we examine different case studies, with special emphasis on vicinal surfaces, in which the symmetry of the elastic field and of pair interactions between islands affects the growth evolution. Finally, in the last section we briefly describe the effect of intermixing on the energy relaxation of nanostructures.

2. Epitaxial growth and elasticity: concepts and definitions

Derived from the Greek language and composed by the prefix *ἐπι* meaning 'over' and *τάξις* meaning 'order', the word epitaxy literally means 'oriented growth of a material onto a different material [9]'. Epitaxial growth can be therefore identified as the process in which a deposit crystal is grown on the single crystal surface of a different substrate crystal. Substrate and deposit may differ either chemically or geometrically. The epitaxial growth of a material A on a substrate B is governed by the surface energies of the overlayer, of the substrate and of the interface. In the following sections, we will mainly discuss the case of SK growth: This process occurs after an initially perfect wetting of the substrate is performed and the surface energy tradeoff is modified. Consequently at a critical thickness, the initial wetting condition is violated and henceforth 3D islands start forming. The most common example of this SK process is when a semiconductor film is epitaxially grown onto a surface of another semiconductor with the same symmetry and crystal structure, but with different lattice parameter. Due to the strain accumulation at the heterojunction interface caused by the lattice mismatch, the film is inherently unstable and, at a certain thickness, the excess elastic strain energy is relieved by surface roughness in the form of coherently strained islands on top of a two-dimensional (2D) wetting-layer (WL).

There are two main sources of strain in heteroepitaxy: (a) the difference in the lattice parameters, and (b) the difference in the thermal expansion coefficient between the epilayer and the substrate. Generally speaking, both parameters have different values in the epitaxial layer and in the substrate; nonetheless the lattice parameter mismatch is generally the most significant. We can confirm this by considering the pivotal case study of Ge/Si. The lattice constants of Si and Ge are $a_{\mathrm{Si}} = 5.428\,\text{Å}$ and $a_{\mathrm{Ge}} = 5.658\,\text{Å}$ [10]. Thus, the lattice mismatch in the Ge/Si system at room temperature is approximately 4×10^{-2}. On the other hand, the linear thermal expansion coefficient of Si and Ge are $2.7 \times 10^{-6}\,\mathrm{K}^{-1}$ and $5.9 \times 10^{-6}\,\mathrm{K}^{-1}$, respectively [10]. This produces a difference in thermal expansion coefficient of Si and Ge of the order of 3.2×10^{-6} and a strain of order $(3.2\times10^{-6})\delta T$ for a temperature change of δT. Therefore, also taking into account a temperature incursion of 1273 K, which corresponds to the maximum practical growth temperature on the Ge/Si system, we conclude that thermal strains are one order of magnitude less than lattice mismatch strains.

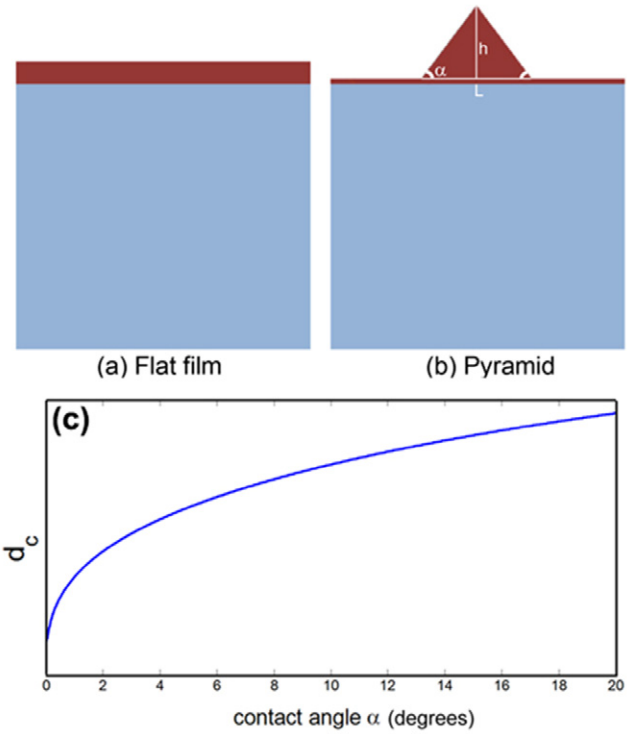

Figure 1. (a,b) For the evaluation of the free energy gain of 3D islanding with respect to a flat film. α is the contact angle of the 3D pyramid of height h and lateral edge L. (c) Critical thickness dc for 3D islanding as a function of the island contact angle α.

When referring to a *coherent* or *pseudomorphic* growth of the overlayer, we mean that the heteroepitaxial layer does not keep its own lattice constant a_e but is tetragonally distorted to the substrate lattice parameter a_s (figure 1). We then define the lattice mismatch f between the substrate and the epilayer as $f = (a_e - a_s)/a_e$ [11]. If we now assume that the lattice parameter difference is accommodated entirely elastically, i.e. without the formation of misfit dislocations, and if we also neglect the effects of differential thermal expansion coefficients we can then directly link the elastic strain of the epilayer in the plane of the interface with the lattice mismatch:

$$\varepsilon_{\parallel} = 2\frac{(a_s - a_e)}{(a_e + a_s)} \approx \frac{(a_s - a_e)}{a_e} = -f, \tag{1}$$

From the above equation, we can distinguish between two different cases: (a) For $a_e > a_s$, as in the case of Ge/Si, the strain in the epitaxial layer is compressive and $\varepsilon_{\parallel}$ is negative and (b) for $a_e < a_s$, the film is stretched and the in-plane strain is tensile ($\varepsilon_{\parallel} > 0$). Due to the biaxial in-plane distortion, the epitaxial layer relaxes along the interface normal and produces an out-of-plane strain component

$$\varepsilon_{\perp} = 2\frac{\nu}{(1-\nu)}f, \tag{2}$$

where ν is the Poisson ratio of the epilayer material. In other words, the biaxial compression within the pseudomorphic Ge layers grown on Si induces an outward distortion in the growth

direction. For $\nu_{Ge} = 0.273$, one finds that the lattice constant of a Ge film along the interface normal is about 3% larger.

The elastic strain energy per unit area stored in the epitaxial film is defined as

$$\Xi_{el} = \frac{E}{(1-\nu)}\varepsilon_{\parallel}^2 d, \tag{3}$$

where E is the Young's modulus and d the film thickness. For a pure Ge ($x = 1$) epilayer on Si(0 0 1) surface, we have $E \sim 103$ GPa [10] and therefore an elastic energy density $\rho_{2D} = E\varepsilon_{\parallel}^2/(1-\nu)$ of about 1.55 meV Å^{-3}. With an epilayer thickness of 4 ML (∼6 Å), this produces a surface strain energy of ∼10 meV Å^{-2} close to the magnitude of the surface energies densities [12]. Since the elastic energy increases linearly with layer thickness, we therefore expect that such energy can possibly drive the 2D-to-3D growth transition.

The critical thickness d_c at which islanding takes place is of course one of the most important parameters which define a given epitaxial system. This thickness can be determined by examining the free energy balance of a planar epilayer film of area S_{film} and volume V with respect to a configuration in which an island of the same volume is formed on a very thin 2D WL [13–15] (figure 1). The total free energy of the 2D configuration (figure 1(a)) is

$$F_{2D} = \frac{E}{(1-\nu)}\varepsilon_{\parallel}^2 V + (\sigma + \sigma_i)\, S_{film}, \tag{4}$$

where the first term gives the elastic strain energy and the second term gives the surface energy. σ and σ_i are the surface energy densities of the film and the island-substrate interface, respectively. For the configuration of figure 1(b), the total free energy is instead

$$F_{3D} = R\frac{E}{(1-\nu)}\varepsilon_{\parallel}^2 V + (\sigma + \sigma_i)\, S_{film} + \gamma S - \sigma B, \tag{5}$$

where γ is the specific free energy of the island facets of area S and B the base area. Since the formation of a 3D island enables the elastic relaxation of strain, the elastic energy term in equation (5) is reduced by a factor $R < 1$ with respect to the planar film. It follows that the tradeoff between the 3D and the 2D configurations is

$$\Delta F = (R-1)\frac{E}{(1-\nu)}\varepsilon_{\parallel}^2 V + \gamma S - \sigma B. \tag{6}$$

Incidentally, we note that edge energies of the island, scaling as $V^{1/3}$, have been omitted in equations (5) and (6). What makes this tradeoff difficult to calculate in practice is that both the surface energy cost and the strain energy relaxation due to island formation inherently depend on the island shape. Moreover, σ depends sensitively on the film thickness d. In the case of SK growth, this is mainly due to the effect of lattice distortion and, to a lesser extent, to the chemical contribution of the interface energy. A proper description of this issue entails a detailed knowledge of the atomistic structure of surface atom bonding via first-principles calculations [16–18]. In addition, the origin of the critical thickness d_c for islanding has been discussed in connection to the occurrence of intermixing, surface diffusion and segregation [19].

For purposes of simplification we consider a regular square-based pyramid with facet inclination α. The base and lateral surface areas of the islands are defined in terms of the island volume and we assume, for concreteness, $\gamma = \sigma$. After this treatment, the tradeoff becomes

$$\Delta F = (R-1)\frac{E}{(1-\nu)}\varepsilon_{\parallel}^2 V + \gamma\left(\frac{6}{\tan\alpha}\right)^{2/3}(\sec\alpha - 1)\, V^{2/3}. \tag{7}$$

3D-to-2D islanding occurs when F_{2D} becomes larger than F_{3D}, namely at the critical film volume V_c for which $\Delta F = 0$. Thus, the critical thickness at which islanding takes place can be estimated as

$$d_c = V_c^{1/3} = \frac{\Delta F_s\,(1-\nu)}{(1-R)\,E\varepsilon_{\parallel}^2}, \tag{8}$$

where we write $\Delta F_s = \gamma\,(6/\tan\alpha)^{2/3}\,(\sec\alpha - 1)$ for compactness. It has been shown that, for very shallow islands, the elastic problem has an approximate solution $(1-R) \propto \tan(\alpha)$ [13–15, 20]. If we make use of this approximation, we obtain the behavior of d_c as a function of the contact angle of the island facets which is shown in figure 1(c). The vertical axis is displayed in arbitrary units, since a quantitative estimate is beyond the limits of this oversimplified model. Nevertheless, the plot shows that the evolutionary path for the 2D-to-3D transition is one for which the contact angle increases continuously from planar to a 3D morphology [21, 22]. This can be explained as follows. The surface free-energy term ΔF_s, causing the formation of a 3D morphology to be an activated process, scales with the sidewall angle of the islands. This means that, when the morphology is shallower, less new surface is created, and hence the activation energy is also lower. As shown by scanning tunneling microscopy (STM) measurements shown in figure 2, this *continuous* islanding process is experimentally observed in Ge/Si heteroepitaxy and occurs between 3.2 and 3.8 monolayers (MLs) of Ge (1 ML = 1.4 Å) [21, 23–26]. From the images, it can be seen that the initial step of the 3D transition takes place via the formation of shallow mounds, with a height-to-base ratio ranging between 0.015 and 0.03, which become progressively larger and steeper, finally evolving into complete square-base pyramids bounded by facets [1].

The cost to be paid, in order to obtain more quantitative information, is the mathematical simplicity of isotropic elasticity. In fact, silicon and germanium are highly anisotropic materials, with elastic behavior dependent on the crystal orientation. For example, the possible values of the Young's modulus for Si range from 130 to 188 GPa [27] and, hence, the use of an average elastic constant is a significant approximation producing errors of an order of 10–20%. Therefore, we cannot avoid making use of complete anisotropic description in the following analysis.

Hooke's law- i.e. the fundamental law of linear elasticity- describes the relationship between stress σ and strain ε in terms of stiffness $\boldsymbol{C}$

$$\sigma = C\varepsilon. \tag{9}$$

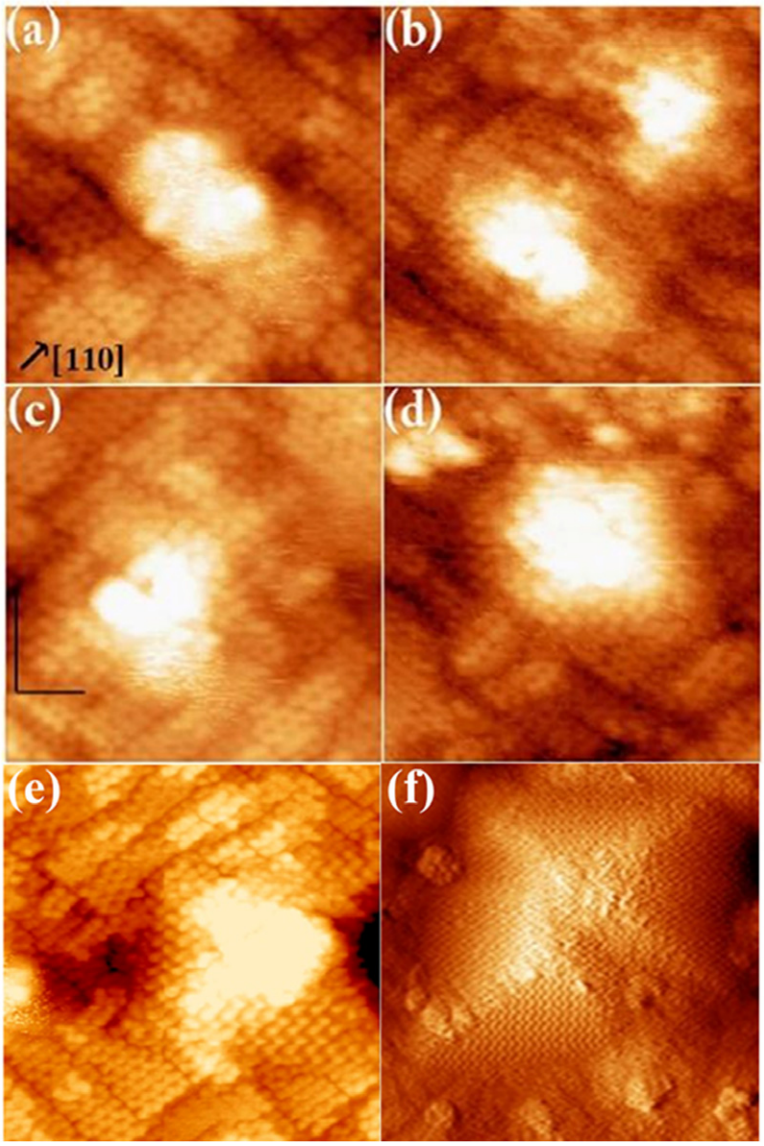

Figure 2. STM images ($25 \times 25\,\text{nm}^2$) showing the formation of the first Ge 3D islands on the Si(0 0 1) surface.

For isotropic uniaxial crystals, the stiffness C is a single value parameter known as Young's modulus E. In an anisotropic material, things are not so simple and the stiffness is represented by a fourth rank tensor with $3^4 = 81$ terms. In this case, Hooke's law is written as

$$\sigma_{ij} = C_{ijkl}\varepsilon_{kl}. \tag{10}$$

Note that all indices span between 1 and 3 and that the sum over repeated indices is understood. In cubic semiconductors, such as Si and Ge, only three independent components are needed to describe the complex stiffness tensor; their values are summarized in table 1.

For the (0 0 1) crystal plane, the Poisson ratio and the Young's modulus, written in terms of the anisotropic elastic constants become

$$\nu_{001} = \frac{C_{12}}{(C_{11}+C_{12})}; \quad E_{001} = \frac{(C_{11}-C_{12})\,(C_{11}+2C_{12})}{(C_{11}+C_{12})} \tag{11}$$

Table 1. Elastic properties of Si and Ge.

Element	Si	Ge
Lattice constant: a	5.428 Å	5.658 Å
Elastic moduli: C_{11}	166.2 GPa	128.4 GPa
C_{12}	64.4 GPa	48.2 GPa
C_{44}	79.8 GPa	66.7 GPa

and the elastic strain energy per unit area (equation (3)) of an anisotropic planar epitaxial film is

$$\Xi_{\text{el}} = \left[C_{11} + C_{12} - 2\frac{C_{12}^2}{C_{11}}\right]\varepsilon_{\parallel}^2 d. \tag{12}$$

The challenge which remains, however, is how to accurately evaluate the elastic relaxation for realistic 3D island's shapes. Several approaches have been proposed for semiconductor QDs. Continuum models may be used to take advantage of the fast, semi-quantitative estimates of analytical solutions.

Continuum models are generally based on Green's functions and are usually described by a flow-chart similar to the following: the elastic field of a macroscopic island is computed starting from the Green function of a point-like inclusion of the deposit crystal on a semi-infinite substrate [28], i.e. integrating this function over the island volume. A very common method developed in this framework is known as *flat-island approximation* [14, 29]. We have already used it to obtain the estimate of R giving the qualitative behavior of d_c in figure 1(c). Unfortunately, the method fails in determining the elastic fields in steep islands, even if a proposed improvement has been shown to yield consistent estimates for this case also [30]. What really limits the application of analytical solutions is that they can be computed for simple island shapes only.

2.1. Finite element simulations for realistic modeling of the elastic properties in epitaxial nanostructures

The complexity of realistic 3D geometry requires the 'brute force' of the computational power of numeric simulations. The two most common computational approaches for studying strain energy relaxation in QD structures are molecular dynamics (MD) and FE methods. As an atomistic approach, MD computes the strain distribution on the basis of the interactions and the displacements of single atoms in the system. This means that atomic-scale features of the system such as surface reconstructions, or inhomogeneous alloying [31–37] are inherently included in the model. On the other hand, such an atomistic approach is computationally very demanding when treating systems, like semiconductor QDs, which consist of several millions of atoms. For this scale, FE simulations offer much more readily accessible results [38–40] which have been shown to be robust and reliable by comparison with atomistic calculations [41].

The basic assumption of FE calculations is that the elastic body can be approximated by an assemblage of discrete elements (typically a tetrahedron for 3D problems). This set of elements, together with their vertices (*nodes*) constitute the finite *mesh*. It is usually convenient to use a non-uniform distribution of the mesh elements, i.e. increasing the density where the elastic energy is expected to be higher—i.e. inside the island. In this case, any field variable $f(r)$ will be completely defined by its nodal values and by the interpolation functions within the elements.

Let us now apply the FE approach to an epitaxial model system, i.e. a depositing crystal in the shape of a pyramid grown on a substrate with smaller lattice parameter (figure 3). The initial condition for the strain is set by the lattice mismatch f: before relaxation, the deposit is compressively strained to the substrate lattice parameter in the three perpendicular directions (in plane x and y, and out-of-plane z) and the initial condition thus reads $\varepsilon_{xx} = \varepsilon_{yy} = \varepsilon_{zz} = -f$, where ε_{xx}, ε_{yy} and ε_{zz} represent the three diagonal components of the strain tensor. Now the best way needs to be found to mimic the lattice mismatch in the framework of continuum elasticity [42]. The solution is to adopt the so-called Eshelby formalism for inclusions [43]. We define this as an *inclusion*

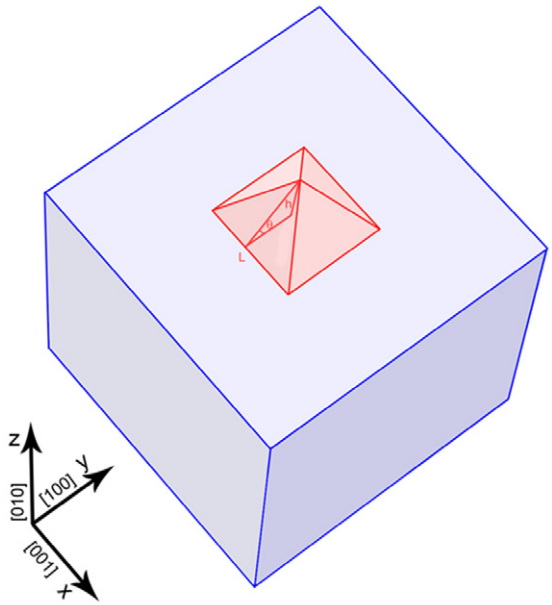

Figure 3. Geometric model of a Ge pyramid on a Si(0 0 1) substrate used in FE simulations. Copyright Wiley-VCH Verlag GmbH & Co. Reproduced with permission [11].

of a region, completely embedded in a surrounding medium (*matrix*), which undergoes a permanent deformation. If we now remove the inclusion from the medium, the medium will experience a deformation so as to restore the zero-stress condition, assuming a uniform strain ε^*_{ij} called *eigenstrain*. Therefore, the eigenstrain is defined as the value of the strain field at which the stress field is zero by the following equation

$$\sigma_{ij} = C_{ijkl}\left(\varepsilon_{kl} - \varepsilon^*_{kl}\right). \tag{13}$$

In our case, since the island itself acts as a stressor and if we were able to take the compressed island away from the substrate, it would undergo an elastic dilation, according to the eigenstrain principle, to recover its own lattice parameter. As a consequence the eigenstrain is simply

$$\varepsilon^*_{kl} = f\delta_{kl}, \tag{14}$$

where δ_{ij} is the Kronecker delta. In the real world, the state of eigenstrain—i.e. the condition of zero stress—is never reached by the island; conversely both the substrate and the island deform in order to minimize the elastic energy. Solving the elastic problem means finding the displacement field caused by the condition of eigenstrain in the entire space. Therefore, the minimum elastic-energy distribution can be obtained by allowing the system to relax, as far as the elastic equilibrium is reached. The equilibrium condition is defined by the following requirement: the sum of forces inside the elastic body has to balance the external force T_i acting on it; thus the equilibrium equation can be written as

$$-\frac{\partial}{\partial x_j}\sigma_{ij}(u) = T_i, \tag{15}$$

where u is the displacement field. The island itself being at the origin of the stress in the system, and there are no external

forces, so $T_i = 0$. By looking at figure 3, we can define different types of boundary conditions. With the exception of the bottom of the simulation box where the Dirichlet condition $u_i = 0$ is imposed, all the other boundaries are free surfaces at which the null-stress condition $\boldsymbol{\sigma}\cdot\boldsymbol{n} = 0$ holds ($\boldsymbol{n}$ is the normal to any free surface). In addition, we apply periodic boundary conditions (PBCs) in the x–y plane in order to simulate an infinite bulk.

The elastic problem described by equation (15) is solved self-consistently by using the constitutive stress-strain relations (13) and (14) which, for a cubic symmetry, are

$$\begin{aligned}\sigma_{ii} &= (C_{11} - C_{12})\varepsilon_{ii} + C_{12} f \\ \sigma_{ij} &= C_{44}\varepsilon_{ij} (\mathrm{i} \neq \mathrm{j}).\end{aligned} \tag{16}$$

By means of an iterative procedure, the FE solver looks for the displacement field u minimizing the elastic energy (per unit volume) of the system $\rho = \frac{1}{2}\sum_{klmn} C_{klmn}\varepsilon_{kl}\varepsilon_{mn}$ which, for structure with cubic structure, reduces to

$$\begin{aligned}\rho = \frac{C_{11}}{2}\left(\varepsilon_{xx}^2 + \varepsilon_{yy}^2 + \varepsilon_{zz}^2\right) + 2C_{44}\left(\varepsilon_{xy}^2 + \varepsilon_{yz}^2 + \varepsilon_{xz}^2\right) \\ +2C_{12}\left(\varepsilon_{xx}\varepsilon_{yy} + \varepsilon_{xx}\varepsilon_{zz} + \varepsilon_{yy}\varepsilon_{zz}\right).\end{aligned} \tag{17}$$

After minimization, the total elastic energy of the system is computed by integrating the local energy density over the island and the substrate volumes

$$\rho_{3D} V = \left[\int_{\mathrm{isl}} \rho\,(\boldsymbol{r})\mathrm{d}r + \int_{\mathrm{sub}} \rho\,(\boldsymbol{r})\mathrm{d}r\right]. \tag{18}$$

As the reader may have noticed, we completely neglected the thin WL under the island in the previous description. Introducing a very thin layer in FE calculations is higly problematical: first, it requires a high number of mesh elements, increasing significantly the computational effort. Moreover, FE simulation including the WL is not fully self-similar, since the thickness of the WL is fixed (e.g. 3–4 ML for Ge/Si) independently of the island size; therefore, its weight over the elastic body depends on the island volume. The question to be answered is: can we afford to neglect the WL in the simulations? We can obtain a rough estimate of the weight of WL by evaluating the total energy E_{sub} stored in the substrate (i.e. the second integral in equation (18)) with and without this thin planar epilayer.

In figure 4, the normalized change of E_{sub} has been calculated for Ge/Si pyramids having the same volume but with a different facet inclination. As is evident, the WL plays a role in the elastic relaxation of the system only for very shallow island morphology. Steeper islands, in fact, exert an elastic loading deeper in the substrate and, as such, the presence of the WL becomes in this case negligible.

2.2. Thermodynamic stability of epitaxial nanostructures

As shown in the previous section, FE simulations offer a straightforward method for computing the relaxation factor R appearing in equation (5) for complex 3D island shapes within anisotropic elasticity. Our goal is now to establish some

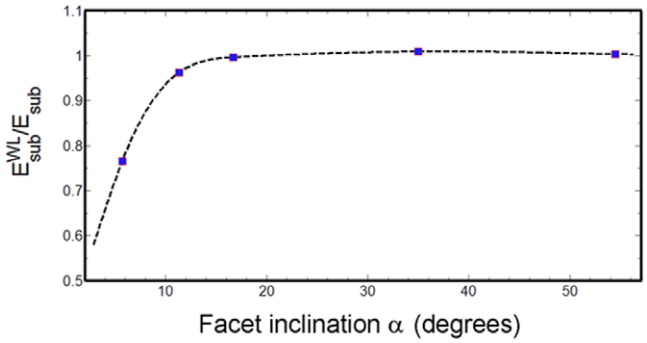

Figure 4. Relative weight of WL in FE simulations as a function of the facet inclination of Ge pyramid. $E^{\mathrm{WL}}_{\mathrm{sub}}$ is the elastic energy stored in the substrate including the WL, whereas E_{sub} is the same term neglecting the presence of the WL. Copyright Wiley-VCH Verlag GmbH & Co. Reproduced with permission [11].

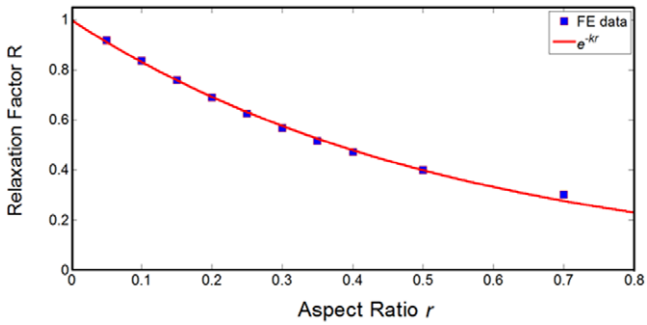

Figure 5. Relaxation factor as a function of the aspect ratio of Ge pyramids. Data obtained by FE calculations (squares) are fitted by an exponential decay curve (continuous line) using $k = 1.839\,\text{Å}^{-1}$. Copyright Wiley-VCH Verlag GmbH & Co. Reproduced with permission [11].

general criteria for the thermodynamic stability of different island shapes. For a direct comparison with experimental data, we define the island geometry in terms of the height to-square-root of the island base ratio or *aspect ratio* r. For square-based pyramids, r is simply $1/2(\tan(\alpha))$. Figure 5 shows the aspect-ratio dependence of the relaxation factor for pure Ge islands grown on the Si(0 0 1) surface. It is immediately noticeable that R decreases monotonically as the facet inclination increases, thus indicating that steeper structures provide a better elastic relaxation. By looking at the distribution of the ε_{xx} strain tensor component inside the islands (figure 6), it can be seen that, for the steeper island, the island top is almost completely relaxed and the compressive distortion is mostly concentrated in the lower part, which is in close proximity to the substrate.

This dependence of the relaxation factor on shape is very general and is not restricted to the pyramid case alone [44]. It is therefore useful to find an analytical form to describe the functional behavior of R with aspect ratio. It has been shown that a simple exponential form $R(r) = \mathrm{e}^{-kr}$ is suitable to fit FE data except at high values of r [45]. For data shown in figure 5, we obtain $k = 1.839\,\text{Å}^{-1}$. It is evident that steep islands provide better elastic relaxation: on the other hand, they exert an elastic load which penetrates more deeply into

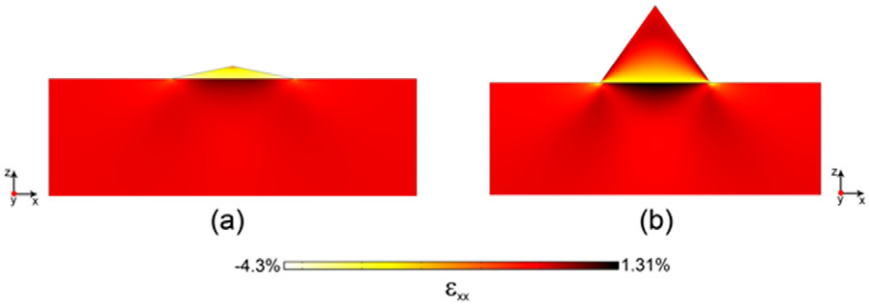

Figure 6. Cross-sectional maps of the ε_{xx} strain component for Ge islands of aspect ratio (a) $r = 0.1$ and (b) $r = 0.7$. Copyright Wiley-VCH Verlag GmbH & Co. Reproduced with permission [11].

the substrate, as shown in figure 6. Note that the effect of substrate loading is correctly taken into account in equation (18), whereas it is neglected by using a single-exponential decay fitting function. To compensate for this bias, one could add a positive exponential $e^{k_2 r}$ factor to $R(r)$ [42].

For the sake of simplicity, we use a single exponential for $R(r)$. This makes it easy to write the total energy difference between the island and planar configurations (equation (7)) in terms of the aspect ratio r

$$\Delta F\,(r, V) = \left(e^{-kr} - 1\right)\rho_{\mathrm{WL}} V + \gamma \left(\frac{3}{r}\right)^{2/3} \left(\sqrt{4r^2+1} - 1\right) \times V^{2/3}, \tag{19}$$

where $\rho_{\mathrm{WL}} = \Xi_{\mathrm{el}}/d$. This equation provides a scaling expression for the energy balance driving the morphological evolution of islands with volume and is useful for comparing the relative thermodynamic stability of different island shapes [45].

For a given volume, the equilibrium aspect ratio corresponds to the minimum of $\Delta F(r)$. We can therefore obtain the shape evolution with volume predicted by thermodynamics by setting $\partial \Delta F\,(r, V)/\partial r = 0$, giving

$$e^{-kr} = \frac{2}{3^{1/3} k} \left(\frac{\gamma}{\rho_{\mathrm{WL}}}\right) \left[\frac{2r^2 - 1 + \sqrt{4r^2+1}}{r^{5/3}\sqrt{4r^2+1}}\right] \frac{1}{V^{1/3}}, \tag{20}$$

and solving equation (20) for different volumes. The results are shown in figure 7(b). Since, in the small-volume limit, the surface cost of islanding is dominant, shallow islands are energetically favored. As the volume grows, the volume term becomes increasingly important; thus, the better elastic relaxation, provided by steeper morphologies, counterbalances the larger exposed surface.

This morphological evolution of strained epitaxial nanostructures towards steeper shapes at larger volumes is experimentally observed for a variety of semiconductor epitaxial systems [7]. As an example, we consider the Ge/Si(0 0 1) system. Figure 8 shows experimental values of the aspect ratio as a function of volume for Ge islands grown on the Si(0 0 1) surface at 600 °C. As expected, the general trend shows that the larger the island, the steeper is the island's facet inclination. However, a close inspection of the experimental plot shows sudden slope changes at characteristic islands volumes superimposed on the monotonic increase of the r curve. Obviously, these features should correspond to

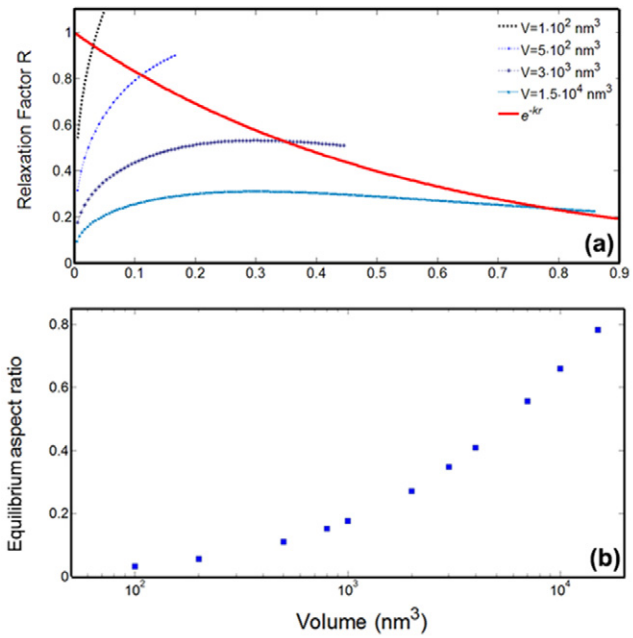

Figure 7. (a) Equilibrium relaxation factor as a function of aspect ratio at increasing volume as a graphical solution of equation (20). (b) Thermodynamically favored island's aspect ratio as a function of volume. The squares correspond to the solution of equation (20) for different volumes. Copyright Wiley-VCH Verlag GmbH & Co. Reproduced with permission [11].

distinct morphological transitions in the islands shape. In fact, in our oversimplified picture, we have assumed pyramid shapes only, but, actually, also the overall geometry of islands evolves as the Ge growth proceeds. This is clearly shown in figure 9 where the main islands' morphologies observed in Ge/Si(0 0 1) are displayed. Experiments show that, at the onset of 3D islanding, very shallow mounds, known as *pre-pyramids* [24, 26], are formed (figure 9(a)). These structures have a very low aspect ratio ∼0.04 and, above all, are non-faceted. A useful tool for studying island faceting is the so-called facet plot (FP) analysis [46]. It consists of a 2D histogram displaying the component of the surface gradient on the horizontal and vertical axes: Well-defined spots in the FP therefore indicate faceting. Conversely, a diffuse halo, like the one shown in figure 9(b), means that pre-pyramids do not contain distinct facets. At bigger Ge coverage, non-faceted islands evolve into square-based pyramids (figure 9(c)) [25].

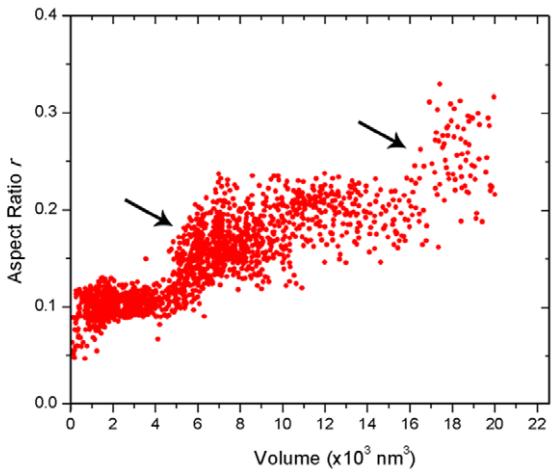

Figure 8. Experimental evolution of island's aspect ratio with volume. Arrows point to the discontinuities which indicate a shape change in the islands. Copyright Wiley-VCH Verlag GmbH & Co. Reproduced with permission [11].

As shown in panel (d), pyramids are bounded by four $\{1\,0\,5\}$ facets forming angle of $\sim 11^\circ$ with the $(0\,0\,1)$ plane ($r = 0.1$).

Faceting is a clear indication of anisotropic surface energy; thus it is inconsistent with the assumption $\gamma = \sigma$ made in equation (7). In the case of the $\{1\,0\,5\}$-faceting in Ge/Si$(0\,0\,1)$ system, in particular, including surface energy anisotropy is crucial when matching quantitatively the experimental results. The $(1\,0\,5)$ surface energy is, in fact, severely lowered for compressive strain experienced in the Ge/Si heteroepitaxy. This is due to the peculiar features of the rebonded-step (RS) reconstruction observed on $\{1\,0\,5\}$ facets [33, 47–49]. In the RS structure the surface is partitioned into nanoscale $\{0\,0\,1\}$ facets by non-rebonded S_A steps and rebonded S_B steps [48]. As a result, the uppermost dimers in the (2×1) unit cell form the characteristic array of U-shaped structures, organized into zigzag rows orthogonal to the $[0\,1\,0]$ direction which are observed in high-resolution STM images (figure 10). The easiest way to include the surface-energy anisotropy in the total free energy gain of islanding (equation (6)) is to combine FE calculations for the elastic term with *ab initio* density functional theory (DFT) data for the strain-dependency of the $(1\,0\,5)$ surface energy [48]. In other words, it is possible to interpolate *ab initio* results [48] for surface energy versus strain and use this dependence to obtain the surface energy value corresponding to the average value of the strain over each facet provided by FE simulations.

The importance of this correction of surface energy is clearly shown by figure 11 where we compare the formation energy $\Delta F(V)$ (equation (6)) of a $\{1\,0\,5\}$ Ge pyramid ($r = 0.1$) calculated assuming a strain-independent surface energy with that obtained after taking into account the dependence of the energy density γ_{105} of the island facets upon strain. The lowering of surface energy under compressive strain flattens the activation energy for island formation, correctly describing the barrierless nucleation process observed experimentally [21, 25].

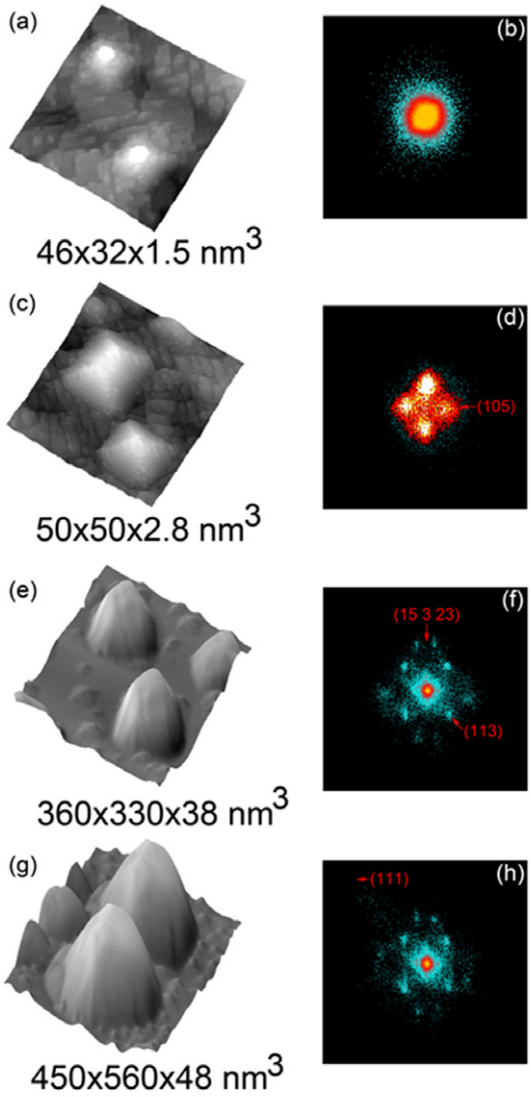

Figure 9. STM images showing the principal islands' morphologies observed in Ge/Si$(0\,0\,1)$ epitaxy: (a) pre-pyramids; (c) pyramids; (e) domes; (g) barns. Panels (b), (d), (f), (h) show the corresponding FPs. Copyright Wiley-VCH Verlag GmbH & Co. Reproduced with permission [11].

A further shape transition, called 'domes', is observed at higher coverage between pyramids and larger islands [50–52]. The domes have a perfect fourfold symmetry like pyramids, but more complex morphology, including four $\{1\,0\,5\}$, four $\{1\,1\,3\}$ and eight $\{15\,3\,23\}$ facets (figure 9(e)). It has been shown that pyramids transform into domes beyond a critical size. Such a transformation is still not fully settled, although the growth sequence of flat pyramid-stepped pyramid-domes starting from the more relaxed top of pyramids seems favored from a kinetic view-point [52]. FE simulations reveal interesting information on this shape transition [16]. Figure 12(a) shows the dependence of $\Delta F(V)$ versus V for pyramids and domes on the singular Si$(0\,0\,1)$ surface. The islands *chemical potential*, μ, figure 12(b), is obtained by differentiating equation (6) with respect to the number of atoms proportional to V. From this analysis, we learn that the shape transition to domes, occurring

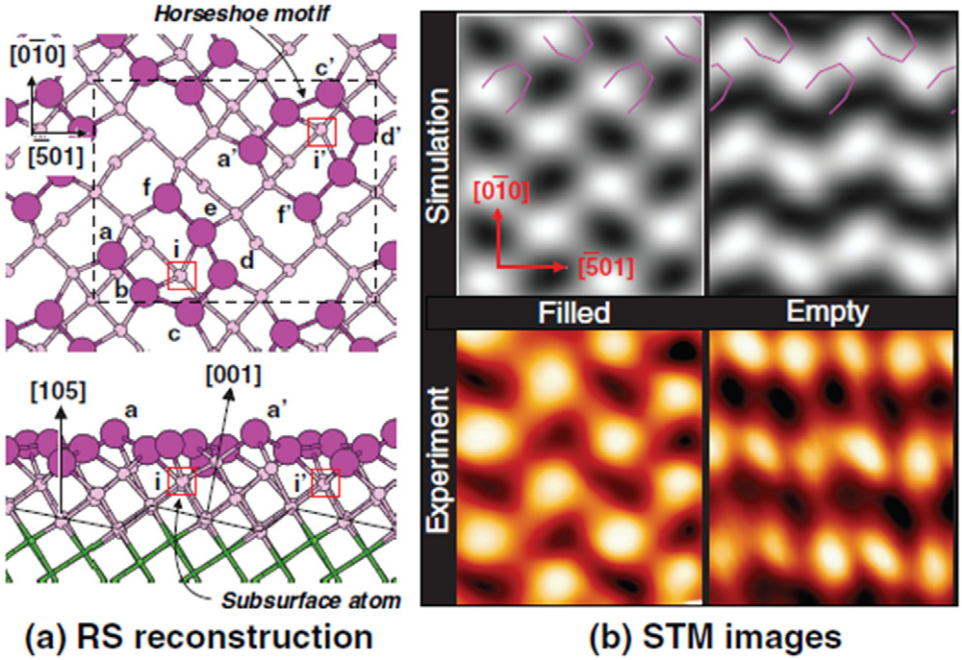

Figure 10. (a) Schematic structure (top and side views) of the Ge/Si(1 0 5) RS surface reconstruction for a 4 ML Ge coverage. Pink circles are Ge; subsurface Si layers are shown below (in green). Dashed lines show the surface unit cell. (b) Experimental and simulated STM images (28 × 33) Å^2 for filled ($V = -1.5$ V; $I = 1.5$ nA) and empty ($V = +1.0$ V; $I = 0.7$ nA) states at constant current. Copyright American Physical Society. Reproduced with permission [84].

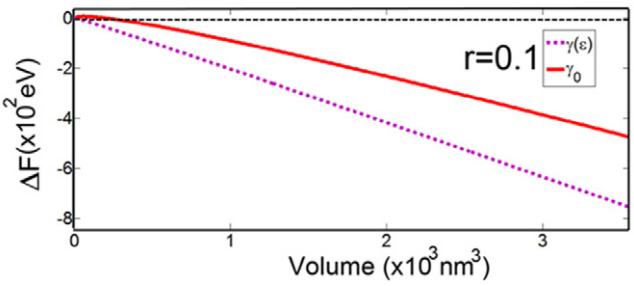

Figure 11. Formation energy of a {1 0 5} Ge pyramid calculated assuming a strain-independent surface energy $\gamma = \sigma = 65$ meV Å^{-2} (continuous line) in comparison to the curve obtained after taking into account the dependence of $\gamma_{\{105\}}$ on strain (dashed line). Adapted from [108].

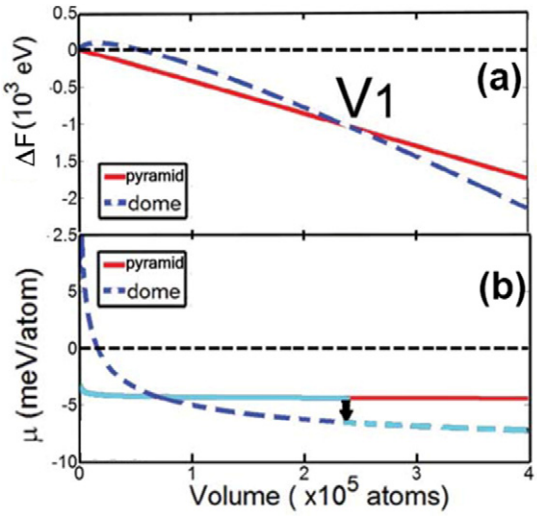

Figure 12. Total energy versus volume for pyramids and domes on the singular surface and the corresponding behavior of chemical potentials. The chemical potential corresponding to the lowest total energy is indicated by the brighter color line showing a discontinuity at the critical volume V_1 marked by the arrow. Adapted from [80].

at the volume V_1, is of the first-order, since it is accompanied by a discontinuity in μ (marked by an arrow).

Recently, another coherent island shape, named *barn* in figure 9(g), has been identified in the high-temperature growth regime ($T = 720\,^\circ$C to 800°) [53, 54]. These islands show a distinct morphology with the appearance of {1 1 1} facets in addition to the facets of domes (figure 9(h)). Stoffel *et al* [54] demonstrated that the transition from domes to barns is very similar to the pyramid-to-dome transition, i.e. the appearance of steeper facets is accompanied by a drop in the area of shallower facets. The formation of barns suggests that steeper facets are progressively stabilized as the growth temperature is increased. This was indeed confirmed by the recent observation of ultra-steep {12 5 3} facets for islands grown at 900 °C [55].

2.3. Island shape and elastic field symmetry

The realistic modeling of the elastic field in epitaxial nanostructures, obtained by FE simulations, makes it possible to directly image the redistribution of elastic energy which drives the formation of 3D islands. In spite of the larger surface area (per unit volume) compared to a flat film, 3D islands are energetically favored due to a global reduction

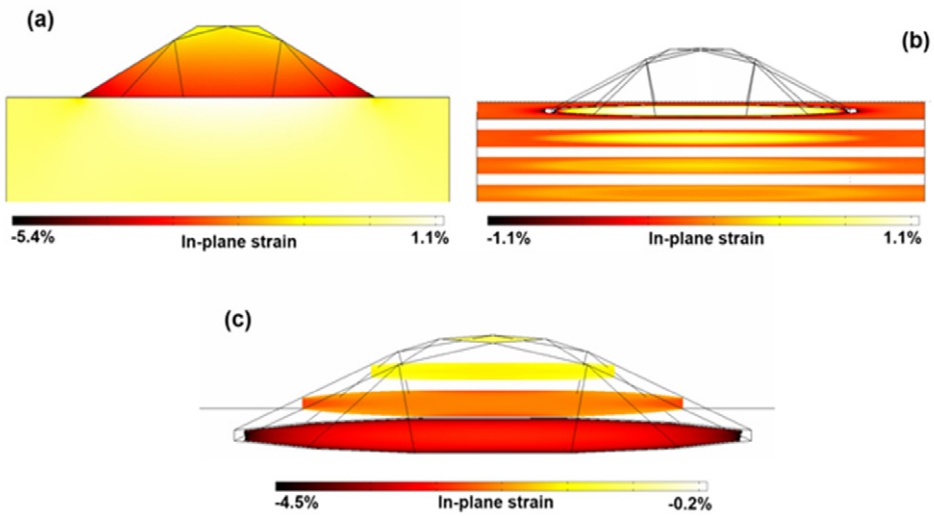

Figure 13. (a) In-plane strain map for a Ge dome grown on a Si(0 0 1) substrate. Panel (b) and (c) show, respectively, cross-sectional slice plots of the strain field in the substrate and the island.

of the elastic energy. Strain relaxation is caused by two simultaneous mechanisms acting in islands [30]. First, misfit strain is not entirely concentrated into the epimaterial, as in the case of a planar film, but is partially redistributed into the substrate. Moreover, on all the free surfaces characterized by an inclination with respect to the interface, the in-plane compression can be partially reduced since the material is free to change its effective lattice parameter forces along the free surface normal (in fact, the forces in that direction vanish). The appearance of a non-uniform elastic field both in the island and in the substrate is clearly evident in figure 13 which shows maps of the in plane-strain $\varepsilon_{\parallel}$ inside a Ge dome and in the Si(0 0 1) substrate underneath. As expected from the lattice parameters of Ge and Si shown in table 1, strain is compressive in the island and tensile in the Si substrate close to the interface. The substrate is partially expanded to match the larger lattice constant of Ge. Clearly, the lattice distortion in the substrate gradually decays as the distance from the island increases (figure 13(b)). Conversely, the island is highly strained close to the base and becomes more and more relaxed, moving from the base towards the top (figure 13(c)). This strain redistribution between island and substrate is evident in figure 14 which shows the average in-plane strain at different position on the vertical axis (normal to the interface). Further interesting details can be obtained by analyzing the detailed shape of the cross-sectional line profiles of $\varepsilon_{\parallel}$ shown in figure 15(a). It is worth noting that the strain profiles in the Ge dome are generally characterized by a higher strain relaxation at the island center, with the exception of the profile on the very top (0 0 1) facet of the dome (topmost continuous profile). At this point it is interesting to highlight the role of the island shape on the strain distribution by discussing the case of Ge/Si(1 1 1) islands. These islands are characterized by a large atomically flat (1 1 1) surface parallel to the substrate plane, and are stabilized by the surface-energy gain [8, 56]. By analyzing figure 15(b), it can be seen that the different island shape determines a completely different strain distribution with

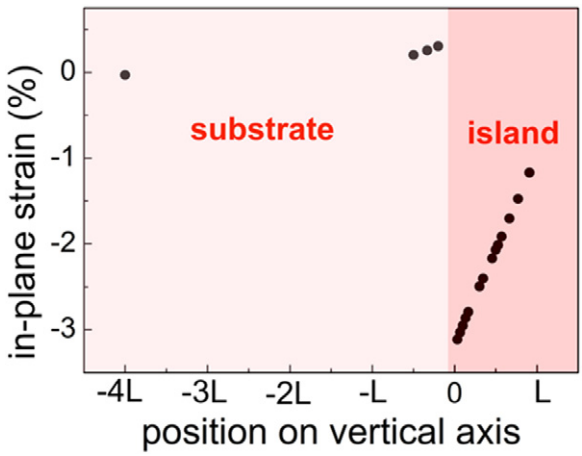

Figure 14. Average in-plane strain at different position on the vertical axis (normal to the interface). The position of the island/substrate interface is at 0. L is the island radius.

respect to the Ge/Si(0 0 1) case: Most of the radial strain profiles in the island now show a maximum compression at the island center. The only exception is the lowest profile drawn at the base of the island: This is due to the higher strain concentration acting at the island base edges.

In the next section, we will discuss a case study in which this peculiar shape-dependent strain profiles of Ge/Si(1 1 1) islands is shown to markedly affect the growth evolution.

3. Experimental case studies

3.1. Strain-biased diffusion in Ge/Si(1 1 1) epitaxy

Epitaxial growth is dominated by the simultaneous effect of elastic and diffusion fields. Therefore, by studying their interconnection, a more exhaustive understanding of the growth process is gained [57, 58]. Experimental and theoretical studies have shown that misfit strain effectively

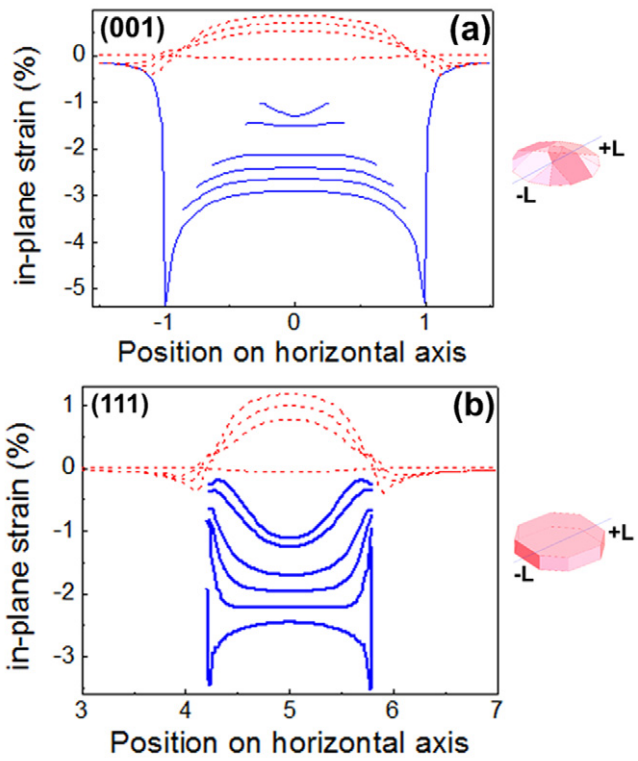

Figure 15. Cross-sectional line profiles of in-plane strain in Ge domes grown on (a) Si(0 0 1) and (b) Si(1 1 1). Profiles are computed for different height in the island and for different depth in the substrate. Continuous lines are the profiles inside the island and dashed lines are the profiles in the substrate. The height and depth at which the profiles refer are given in terms of the island height h. From bottom to top: $h/30$; $h/6$; $h/3.3$; $h/2.2$; $h/1.3$; $h/1.1$; $-4h$; $-h/2$; $-h/3$; $-h/5$.

alters the diffusion pathways by changing the barrier height for diffusion, thus affecting the random motion of individual atoms and determining a net current towards the decreasing strain direction [59].

We have recently highlighted the interdependent role of strain and diffusion on atolls formed after the annealing at high-temperature of large islands grown on a Si(1 1 1) substrate by deposition of 10 ML of Ge at 600 °C [60]. At much larger Ge coverages, ranging between 250 and 1200 ML, and post-growth annealing at 850 °C, a net of continuous corrugations with steep facets on their sidewalls was observed and attributed to the Ge segregation [61].

In this Section we show that, when the elastic field profiles described previously, are coupled to the strain-driven diffusion, the shape evolution from islands to atolls is qualitatively reproduced.

From the experimental standpoint, atolls are formed starting from large singular-top domes annealed to $T \approx 970$ °C for various time intervals. Figure 16 shows Ge atolls formed after 10 s of annealing. They have either triangular or circular bases, resembling the bimodal shape distribution of Ge/Si(1 1 1) islands. From STM images, we observe an outer ridge annulus, on average 30 nm high, separated by a trench-like channel from the internal mesa. Sequential STM images taken as a function of annealing time (figure 17) clearly show the pathway of shape transformation from islands to atolls. Pristine islands are initially indented by the formation of deep trenches around their perimeter growing from the top face down to the substrate and outwards. Trenches are the result of the Ge–Si intermixing caused by the lattice strain on substrate and along the island base and provide an efficient channel for the mass exchange between islands and the substrate through surface transport [62]. As the depression proceeds the inner region of the islands is encircled by surrounding reefs and finally converted into atolls. The result of the highly non-uniform mass transport is clearly observed, the material being drained out from trenches and diffused outwards; as the central mesa is progressively eroded, becoming a shallow mound. The source of this biased diffusion is related to the peculiar strain distribution in Ge/Si(1 1 1). Figure 18 shows a map of the strain energy density ρ (equation (17)), obtained by FE simulations. In line with the strain profiles reported in figure 18(b), the core of the islands is highly strained, whereas a strong misfit relaxation occurs close to the outer rims. In-between, the strain gradient is maximized where the trenches observed in the experiment are formed. This strain gradient originates a flux $J_\rho = -D_\rho \nabla \rho$, where D_ρ is the diffusion coefficient of the process [60]. The strain-driven flux can be added to the general equation for diffusion which reads

$$\partial_t C = D_\rho \nabla^2 \rho + D_C \nabla^2 C. \tag{21}$$

D_C is the ordinary diffusion coefficient of the flux J_C, caused by the gradient of the surface concentration C of Ge adatoms. For a cylindrical island with a highly strained core and an initial aspect ratio of 0.1, we have solved equation (21), modeling the overall shape of the elastic field as $\rho_{n,\omega} \approx e^{-(r^n/n\omega^n)}$, for integer n even and $\omega < 1$. The solution for $\rho_{6,9/16}$ is shown in figure 19.

It should be noted that, at relatively low temperatures ($\leqslant$500 °C) of epitaxial growth, the small diffusion rate of adatoms restricts the influence of intermixing and surface mass transport with respect to the other energy minimization processes. By contrast, these contributions become substantial at higher temperatures and thicker coverage of Ge. As a consequence, a purely kinetic description of the atolls shape evolution seems reasonable as a first approximation. To sum up the gradient of the strain is the source of the diffusion flux driving the formation of atolls. The results shed light on the intimate connection between strain and diffusion, and contribute to a better understanding of their interdependence in the self-assembly of mismatched nanostructures.

3.2. Shaping the morphology by substrate miscut

In the case of a substrate slightly misoriented from a singular plane, the surface breaks up into a staircase of terraces and steps and is referred to as a 'vicinal surface'. The relevant angles of a vicinal surface are the miscut polar angle θ and the azimuthal angle ϕ (figure 20). Tanθ gives the density of steps and tanφ the density of kinks on the step edge [63]. Below we will restrict ourselves to vicinal surfaces with $\phi = 0$ for which the density of kinks is minimal.

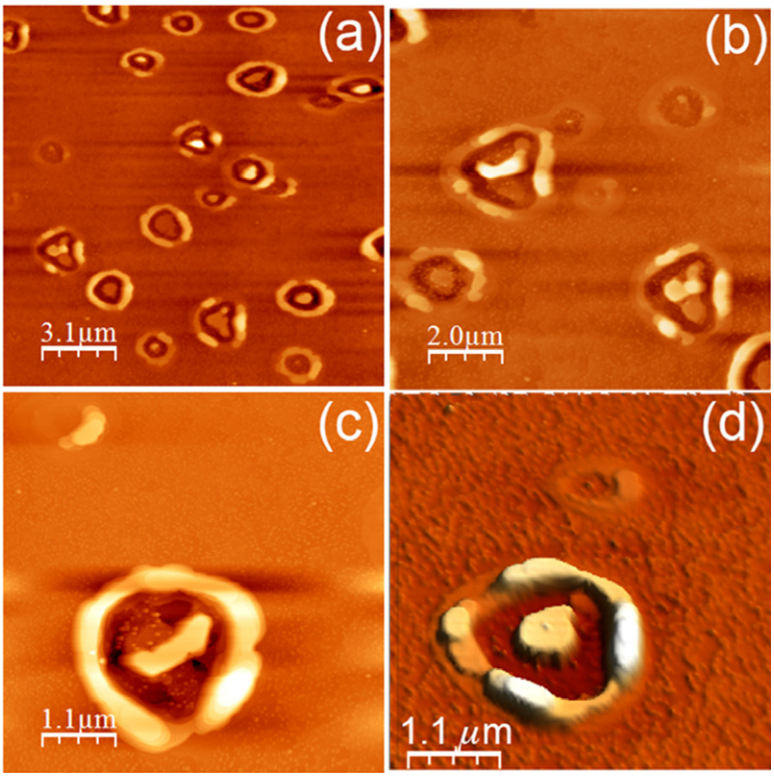

Figure 16. STM images of atolls obtained by 10 s of annealing to 970 °C of 10 ML of Ge grown on the Si(1 1 1) surface. Adapted from [60].

The miscut dependence of vicinal surfaces induces a strong asymmetry in the formation of self-assembled nanostructures [64–66]. Apart from its important implications for the growth process, the broken symmetry is technologically relevant, since it is able to split the degeneracy of electronic levels and to provide optical anisotropy [67–69].

Many investigations have reported extended {1 0 5} faceting on Si(0 0 1) vicinal substrates [65, 69–74], suggesting that the low surface energy of the {1 0 5} plane is crucial in determining the shape evolution of Ge nanoislands. The morphological change of the island is roughly as follows: On the singular Si(0 0 1) surface a {1 0 5} pyramidal island has fourfold symmetry and almost square base with each side oriented along the ⟨0 1 0⟩ directions (figure 21(a)). As the substrate miscut increases, the island elongates along the [1 1 0] direction while its base becomes a distorted rhombus (figure 21(b-e)). This shape change increases the side area of the facets along the step-down direction at the expense of the other facets. Let us consider a pyramid sitting on a vicinal surface (figure 22). The [5 5 1] intersection line of two adjacent {1 0 5} facets is tilted by 8.05° (indicated as $\beta+\theta$ in the sketch) to the (0 0 1) surface. To allow {1 0 5} faceting, this angle must never change, producing the observed elongation toward the miscut direction. The asymmetry in terms of the ratio between the longest and the shortest sides of the pyramid is straightforwardly calculated as

$$\frac{L_{\mathrm{m}}}{L_{\mathrm{M}}} = \sqrt{\frac{\csc^2(8^\circ+\theta)+\csc^2(8^\circ)}{\csc^2(8^\circ-\theta)+\csc^2(8^\circ)}}, \qquad (22)$$

and shown in figure 23 as a function of the miscut angle. The good match between equation (22) and experimental data indicates that the dot asymmetry has a simple geometrical description. FE calculations of the average in-plane strain, $\varepsilon_{xy} = (\varepsilon_{xx+}\varepsilon_{yy})/2$, for a {1 0 5} energy-relaxed pyramid sitting on vicinal surfaces with increasing angles of miscut are illustrated in figure 24. As expected, the Ge pyramid remains for the most extent compressed to match the Si lattice constant even after relaxation. The area nearby the vertex is the most relaxed, but the amount of stress relief decreases as the misorientation angle increases. The reduction of the aspect ratio determines, in fact, a shortening of the apex-substrate distance, thus inhibiting a complete relaxation. The substrate experiences an average low level of strain; some residual tensile strain is observed just below the pyramid, reaching a maximum in correspondence of the projection of pyramid height. To counteract this expansion, the substrate results compressed around pyramid edges.

From a general inspection of the images it is easy to recognize that the higher the value of θ the higher the energy density stored in the pyramid. To be quantitative, the strain energy density, ρ, is computed numerically by integrating over the island and substrate volume and is plotted in figure 25. As anticipated, the elastic energy density inside the island is an increasing function of θ. The amount of energy stored in the substrate, normalized to the island volume, is instead observed to decrease as the pyramid flattens and its capacity of exerting tensile stress diminishes. The total energy density is then obtained by summing up these two terms.

A similar calculation is performed on a thin WL of Ge properly resized in order to cover the uppermost surface of the substrate. By taking PBCs in the x–y plane, in-plane relaxation is inhibited and the film is allowed to relax only along the z

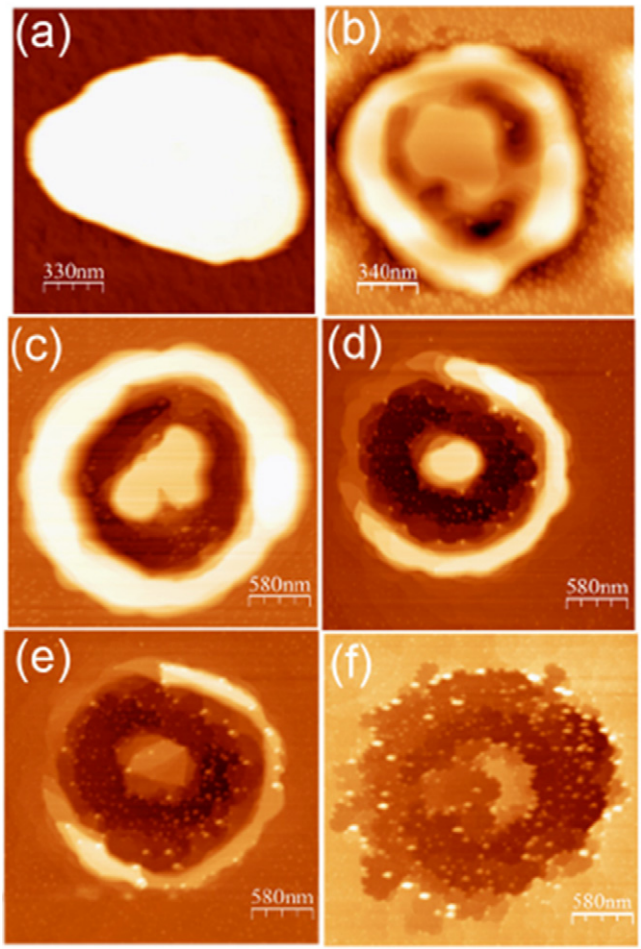

Figure 17. STM snapshots of the shape evolution during annealing to 970 °C: (a) pristine compact islands grown with 10 ML of Ge coverage; (b) 2 s of annealing; (c) 10 s of annealing; (d) 25 s of annealing; (e) 50 s of annealing; (f) 90 s of annealing. Adapted from [60].

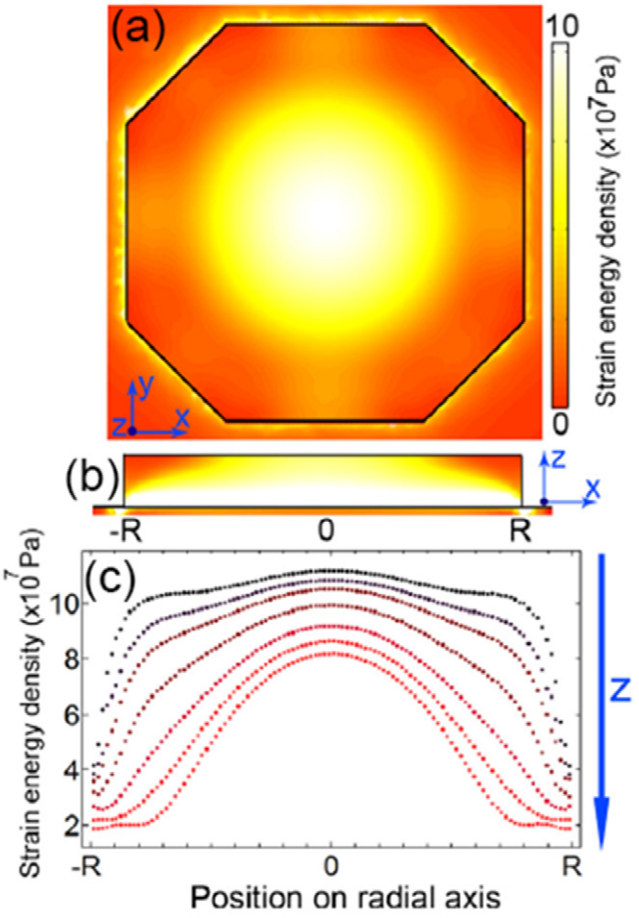

Figure 18. Maps of the strain energy density obtained by FE simulations for Ge/Si(1 1 1) islands: (a) top view; (b) lateral view. R is the island radius. (c) Cross-sectional cuts of the strain maps taken at different heights along the radial diameter of the island. From bottom to top: h; 0.8 h; 0.65 h; 0.5 h; 0.4 h; 0.35 h; 0.3 h. Adapted from [60].

direction. In this way the results are fully independent of WL thickness, provided specific quantities are used. As done for the pyramid, the substrate-WL system is rotated rigidly of an angle θ to simulate an epilayer grown on a vicinal substrate. The calculated ρ function of the WL is shown in figure 25. Unlike pyramid, the substrate has an elastic energy density several orders of magnitude smaller than the WL. Because it lacks Ge-free areas, expanded and compressed domains are no longer possible, and, consequently, no deformation takes place. On the other hand, the amount of elastic energy in the WL is higher than in the pyramid and nearly constant with θ because the amount of energy depends on in-plane elastic constants and the WL does not change its shape according to angle.

Of course, a strict correlation exists between the morphological evolution and the energetics of {1 0 5} facets. The excess (free) energy of the island is derived as in equation (6) with proper allowance for the angular dependence

$$\Delta F\,(V,\theta) = \left(\rho_{\rm pyr}(\theta) - \rho_{\rm WL}(\theta)\right) V + \left[\gamma_{105}{\rm S}(\theta) - \sigma_{\rm WL}(\theta)B(\theta)\right] V^{2/3}. \quad (23)$$

Here, S(θ) and B(θ) are the lateral and base surface areas of the pyramid which are simple increasing functions of the polar angle;

$$\sigma_{\rm WL}(\theta) = \alpha\cos\theta + \beta\sin\theta \quad (24)$$

is the surface energy density of the vicinal Ge WL, which can be estimated from the step formation energy per unit length, β, including [75] or not [64] the step-step interaction energy. $\rho_{\rm pyr}(\theta)$ and $\rho_{\rm WL}(\theta)$ are the elastic-energy densities stored, respectively, in the island (including substrate deformation) and in the WL. In figure 26(a), we plot the total energy versus volume curves for a Ge pyramid grown on a misoriented Si substrate with θ ranging between 0 and 5°. Following Zhang *et al* [76], the following parameters have been used: $\gamma_{105} = 6.0\,{\rm eV\,nm^{-2}}$, $\sigma^{\infty}_{\rm sub} = 8.71{\rm eV\,nm^{-2}}$ and $\sigma^{\infty}_{\rm WL} = 6.05\,{\rm eV\,nm^{-2}}$, where $\sigma^{\infty}_{\rm sub}$ is the surface energy of the bare substrate, and $\sigma^{\infty}_{\rm WL}$ is that of the Ge WL with infinite thickness. The thickness of the WL is $d = 4.5$ ML.

The activation energy for island formation and the critical volume $V_{\rm c}$ corresponding to the maximum of ΔF at a given miscut angle θ are obtained by differentiating equation [23].

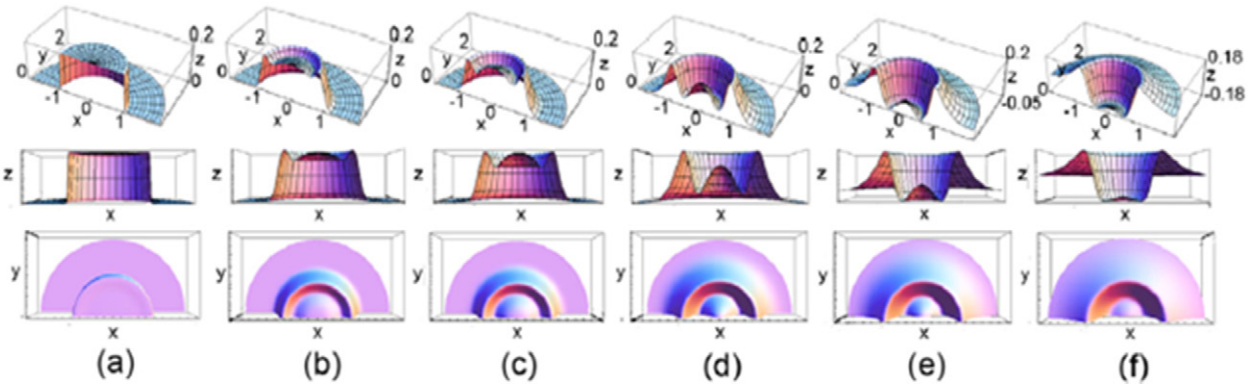

Figure 19. Snapshots of the island shape evolution as obtained by solving the diffusion equation in the presence of misfit strain. t is the simulation time: (a) $t = 0$; (b) $t = 0.005$; (c) $t = 0.01$; (d) $t = 0.05$; (e) $t = 0.1$; (f) $t = 0.2$. Scale boundaries are shown in the uppermost panels. Copyright IOP Science. Reproduced with permission [60].

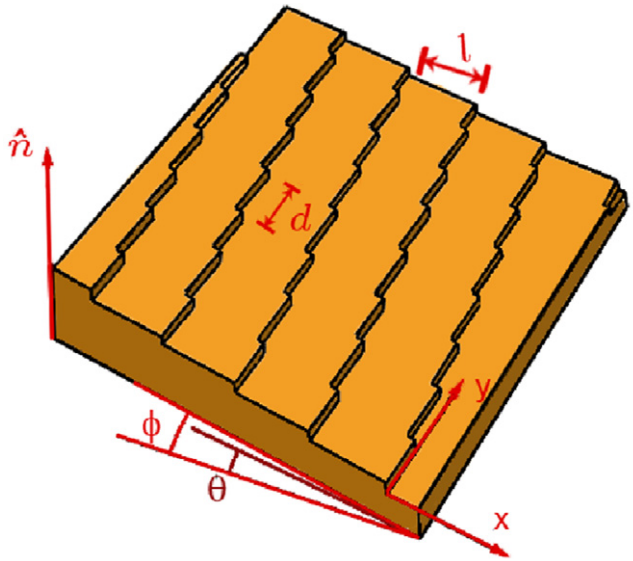

Figure 20. Schematics of a surface vicinal to a high index surface. The density of steps and kinks is determined by the miscut polar angle θ and the azimuthal angle ϕ. l is the average distance between steps and d is the average distance between kinks. Copyright Wiley-VCH Verlag GmbH & Co. Reproduced with permission [11].

With respect to volume and are given by

$$\Delta F_c(\theta) = \frac{4}{27}\frac{\left[\gamma_{105}S(\theta)-\sigma_{WL}(\theta)B(\theta)\right]^3}{\left(\rho_{pyr}(\theta)-\rho_{WL}\right)^2},$$
$$V_c(\theta) = \frac{8}{27}\frac{\left[\gamma_{105}S(\theta)-\sigma_{WL}(\theta)B(\theta)\right]^3}{\left(\rho_{pyr}(\theta)-\rho_{WL}\right)^3}. \quad (25)$$

These quantities are shown in figure 26(b) as a function of θ. One can see that both the nucleation barrier and the island critical volume decrease substantially with the increase in the miscut angle; in other words the nucleation is favored on the vicinal rather than on the singular substrate. Accordingly, a decreased size means fewer atoms form the island and thus there is a smaller fluctuation to start the nucleation process. It is worthy of note that the growth of dots on misoriented substrates results in the progressive decrease of the WL thickness with an increasing of the miscut angle. Nevertheless, the barrier becomes exceedingly large for d thinner than 4 ML ever diminishing probability of nucleating QDs below this coverage, as illustrated in figure 26(c). The theoretical result is consistent with the experimental evidence obtained on vicinal surfaces [74, 77, 78].

When segregation of Ge atoms from the WL to the island is allowed, much more epitaxial material ends up in the QDs on the vicinal than on the singular substrates, causing a strong decrease of V_c at a given critical miscut angle, θ_c , and the WL to disappear [79]. As a consequence, a sharp transition from the SK to the Volmer-Weber growth mode beyond $\theta_c = 4^\circ - 6^\circ$ together with a concomitant increase in the NC density, are predicted. It should be noted, though, that the activation barrier depends strongly on the exact values of γ_{105} and σ_{WL} and that a realistic estimation needs to take into account the strain energy correction to the surface energy [48]. As a result of DFT in the local density approximation, a number of fairly accurate surface energy values for the most relevant GeSi surfaces are available. It is generally found that lowering the surface energy of the {1 0 5} facets under compressive strain flattens the barrier and gives rise to a barrierless nucleation process, observed experimentally on the singular Si(0 0 1) surface [21, 26].

For miscut angles larger than 8.05°, instead, the formation of a pyramid is hindered. As a matter of fact, at $\theta = 8.05^\circ$, the [5 5 1] line runs parallel to the substrate orientation (figure 22) while the island rearranges itself into a strongly elongated prism of triangular cross section bounded by two adjacent {1 0 5} facets called *nanoripple* (figure 27) [65, 73, 80, 81]. Due to the geometric constraint, the down side of the ripple cannot be bounded by real facets; thus it gradually lowers in height and width as the number of stacked {1 0 5} layers decreases near the end of the island (figure 27(b)). An accurate evaluation of the elastic, surface and edge contribution to islanding for $\theta = 8.05^\circ$ shows that it is energetically more convenient to pile up material on a long ripple than to form an additional layer on the WL [82]. This explains the almost perfect alignment of ripples [83] occurring on the Si (1 1 10) surface under Ge deposition (figure 28).

As islands grow, their shape deviates from a skewed version of the symmetric shape becoming asymmetric [80]. In comparison with the domes on the singular surface (figure 29(a)), which have two symmetric {1 1 3} facets along the

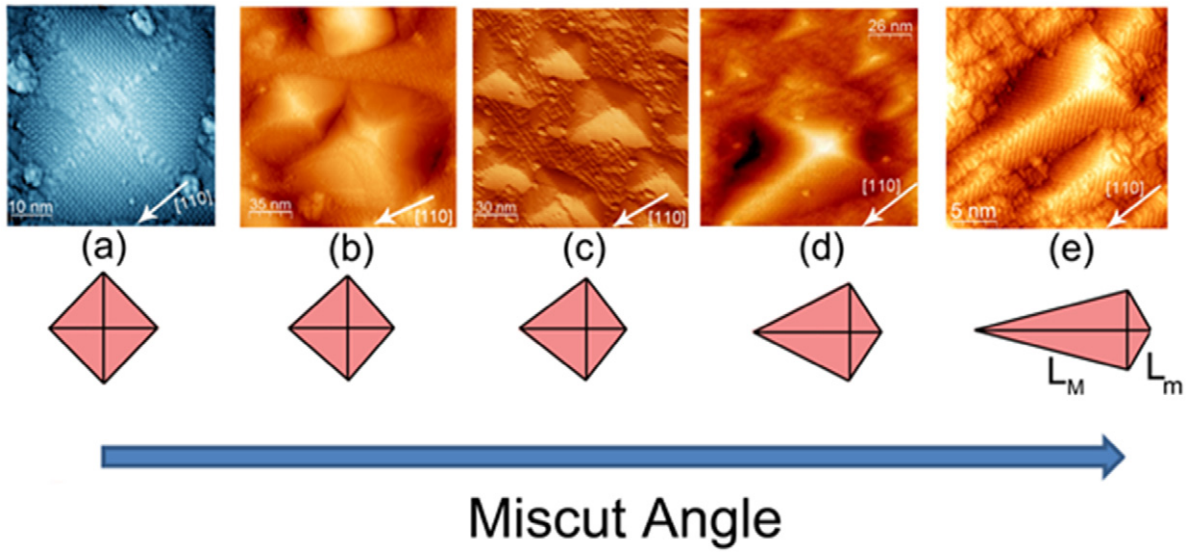

Figure 21. Shape evolution of Ge islands on vicinal Si(0 0 1) surfaces. (a) $\theta = 0°$; (b) $\theta = 1.5°$; (c) $\theta = 2°$; (d) $\theta = 4°$; (e) $\theta = 6°$. From the schematics, it is evident that the perfect fourfold symmetry of square-based islands on the singular surface is broken by the miscut. The miscut-dependent asymmetry can be described in terms of the ratio between the lengths of the shortest (Lm) and the longest (LM) island's sides. Copyright Wiley-VCH Verlag GmbH & Co. Reproduced with permission [11].

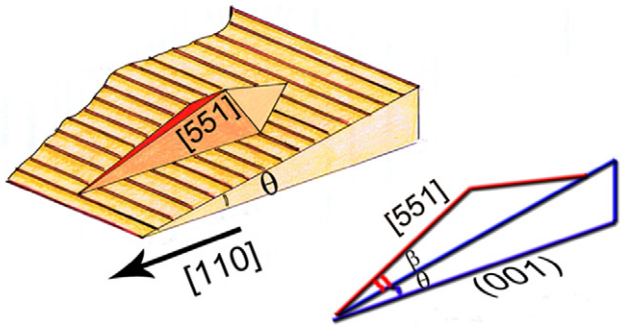

Figure 22. Schematic representation of a {1 0 5} pyramid grown on a vicinal substrate. In the real Stranski–Krastanov growth, a thin WL, not shown in the figure, is present in between the substrate and the pyramid. Copyright Wiley-VCH Verlag GmbH & Co. Reproduced with permission [11].

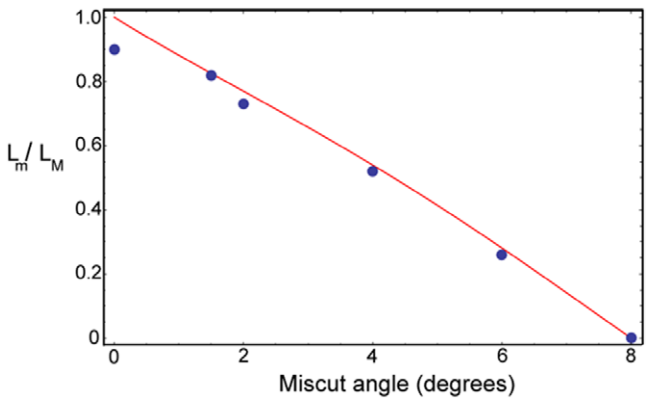

Figure 23. L_m/L_M ratio as a function of the miscut angle. Dots are the experimental values measured from STM images while the continuous line represents the expected analytical ratio for an ideal {1 0 5} pyramid calculated from equation (22). Copyright Wiley-VCH Verlag GmbH & Co. Reproduced with permission [11].

[1 1 0] direction (indicated by α in the corresponding FP), the domes grown on highly miscut substrates have a different set of facets (γ and $\gamma\prime$) on the opposite sides (figure 29(b,c)).

On (0 0 1) substrates with misorientation angles towards the [1 0 0] direction approaching $\theta = 11.3°$ from below, the surface strain causes remarkable changes of the angular dependence of γ, transforming vicinal (0 0 1) surfaces into vicinal surfaces of a *new* singular {1 0 5} face which does not exist on the strain-free equilibrium morphology. This conclusion is illustrated in figure 30 which shows the surface morphology of Si(0 0 1) substrates for $6.0° < \theta < 12.5°$ under increasing deposition of Ge. The left-column STM images show the strain-free arrangement of these surfaces. Up to 6.0–6.5° (figure 30(a) and (d)), when the average width of terraces is comparable to the unit cell size, the (2 × 1) reconstruction of the surface is preserved. However, the long range periodicity is broken by the faceting of steps into a dense array of kinks which compensate for the misorientation along [1 0 0]. Further misorientation destroys the reconstruction resulting for $\theta > 7.5°$ (figure 30 (g) and (l)), in rugged surfaces. The angular constraint $\theta \approx 7.5°$ is set by the width of the smallest (2 × 1) terrace with average ⟨0 1 0⟩ orientation of steps along the [1 1 0] direction and no longer holds in the [1 1 0] direction where stable (0 0 1) surfaces are observed up to $\theta > 10°$. By increasing Ge coverage, the rough (g) and (l) surfaces flatten considerably, exhibiting the terrace-step morphology of a vicinal surface (figure 30(i) and (n)) and the typical RS reconstruction of the {1 0 5} side facets of QDs grown on Si(0 0 1) substrates (figure 30 (h) and (m)). The surface flatness is comparable with that of a singular facet, which is understandable if one notices that, above $\theta = 6.5°$, surfaces are vicinal to the [1 0 5] face with terraces parallel to the (1 0 5) plane rather than to the (0 0 1) plane. Thus a polar angle of, e.g. $\theta = 10.5°$ is only ∼1° off the (1 0 5) plane and, hence, the terraces are wider than those (0 0 1) oriented toward

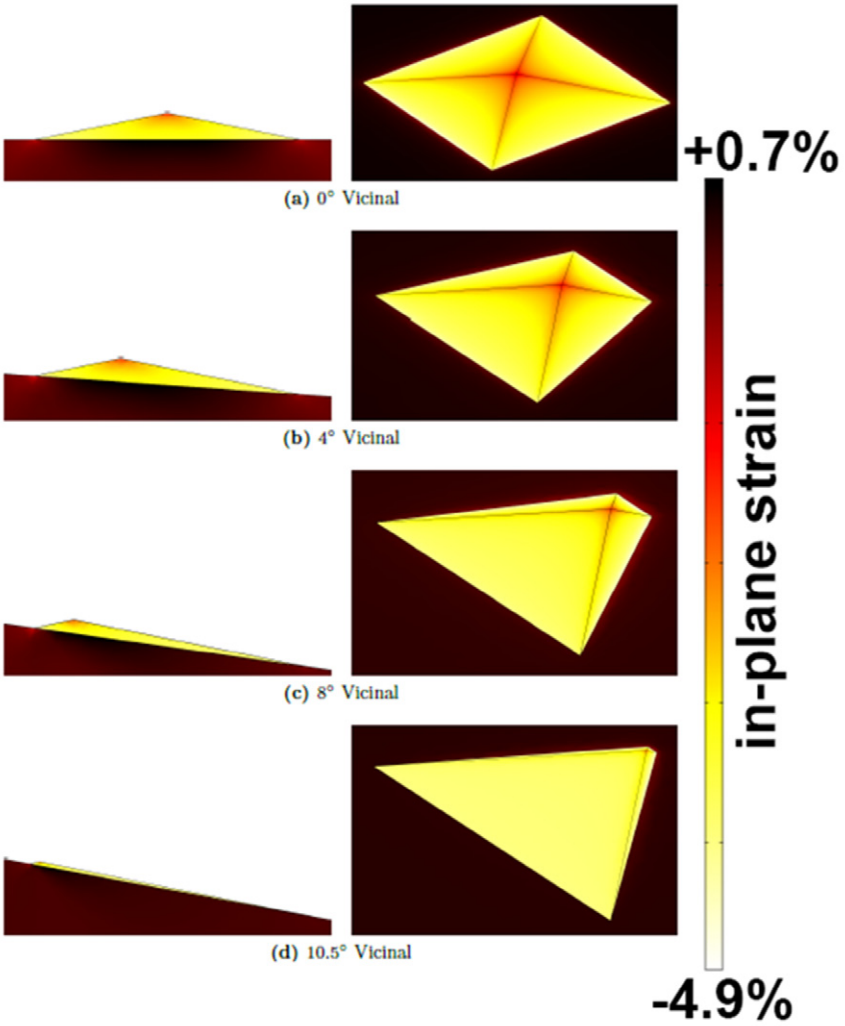

Figure 24. Results of FEM calculations on {1 0 5} pyramidal islands. Left panels: cross section along the highest symmetry direction. Right panels: corresponding 3D view. The chromatic scale gives the negative (compressive) strain experienced by the pyramid and the positive (tensile) strain experienced by the Si substrate.

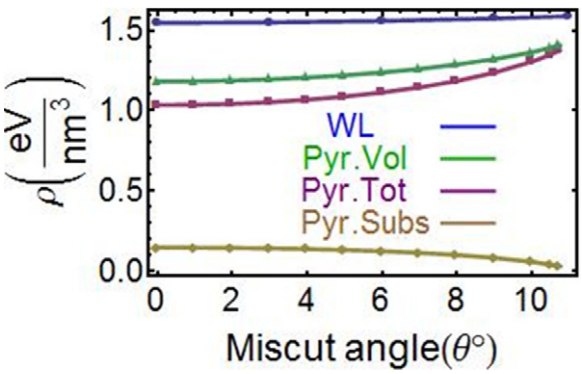

Figure 25. Partial and total contributions to the elastic energy density ρ for the pyramidal island and the WL as a function of miscut angle.

the [1 1 0] direction, as sketched in figure 31 and evidenced by STM images in figure 32. Ultimately, the overall surface morphology is changed since small and highly kinked (0 0 1) terraces are replaced by much larger and regular (1 0 5) terraces (figure 30(n)). This indicates that the (0 0 1)-to-(1 0 5) phase transition is not just a matter of geometry but is also driven by an effective energy gain. Therefore, the large-θ dependence of the surface energy density (equation (23)), for which step-step dipolar interactions can no longer be neglected, must play a crucial role.

A generic vicinal orientation intermediate between the (0 0 1) and the (1 0 5) planes can then be represented as

$$\sigma_{k,\mathrm{WL}}(\theta) = \alpha_k \cos(\theta_k - \theta) + \frac{\beta_k}{h_k}\sin(\theta_i - \theta) + \frac{A}{h_k^3}\frac{\sin^3(\theta_k - \theta)}{\cos^2(\theta_k - \theta)}, \tag{26}$$

where k labels the reference directions σ_{001} $=$ 0° or σ_{105} $=$ 11.3°. The resulting σ-plot, shown in figure 33(a), captures the essential features of the experiment, namely, the appearance of two cusps in the correspondence of the (0 0 1) and the (1 0 5) orientations, the latter acting as a singular face *in the presence of epitaxial strain*. Once strain is introduced through Ge deposition, the (2×1) structure remains favored from $\theta = 0^\circ$ up to $\theta < 5^\circ$ [70]. At larger θ values, the (1 0 5) surface

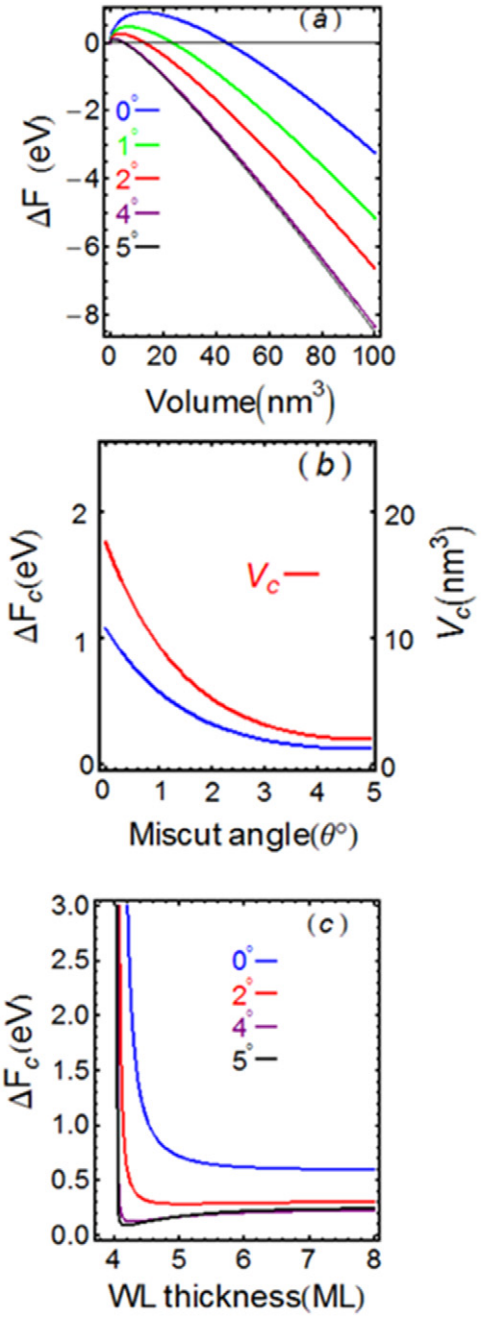

Figure 26. (a) Free energy of pyramidal Ge islands grown on vicinal Si(0 0 1) surfaces as a function of volume for various miscut angles and fixed WL thickness of 4.5 ML. (b) Energy barrier and critical volume as a function of miscut angle. (c) Energy barrier as a function of WL thickness for various miscut angles.

is the most stable and, thus, it develops as follows: (a) at 6.5° it replaces the (2 × 1) reconstruction, and (b) at higher angles it evolves from the initially rough morphology of the clean surface for which the (2 × 1) reconstruction is hindered geometrically toward the vicinal (1 0 5) stepped morphology. Owing to the symmetric shape of the σ-plot around the (1 0 5) cusp, the structural evolution for $\theta = 12.5°$ is the same as at angles slightly lower than 11.3°.

Combining equation (23) and (26) and setting $\sigma_{WL}(\theta) = \gamma_{105}$ for large θ's to mimic the fact that terraces run parallel to the (1 0 5) plane, one finds that islands' nucleation is an activated process on (1 0 5) terraces, as illustrated in figure 33(b). Indeed, experiments show that {1 0 5} islands formed at the earliest stages of growth coexist with domes at larger coverage (figure 34(a)). Due to the misorientation from the (0 0 1) plane, {1 0 5} pyramids have truncated skewed shapes (figure 34(b)). For $\theta > 5°$, the surface energy gain of {1 0 5} pyramids is counterbalanced by that of the {1 0 5}-reconstructed planar WL. At low Ge coverage, the activated nucleation of pyramids requires large fluctuations to form clusters of critical size; this is definitely not a plausible kinetic route compared to the thickening of a low-surface-energy 2D film. At larger coverage, instead, the system is prone to choose the steeper dome shape to relieve strain efficiently.

The emergence of a strain-induced branch in the σ-plot of the substrate delays the onset of 3D islanding from about 3.5 to 5 ML, above which only domes grow (figure 34(c)). Indeed, the aspect ratio distribution on the 6°-miscut (0 0 1) surface is unimodal (figure 34(e)). Also the pathway leading to domes is different: domes, which usually develop from increasingly steeper pyramids, evolve from seeds nucleated onto planar WL (figure 34(d)). This shows that on vicinal surfaces strain-induced structural changes result in huge alterations of the SK growth, leading to the equilibrium phase diagram displayed in figure 35. The diagram schematically summarizes the above results. The most striking feature is the appearance of the RS (1 0 5) reconstruction in the narrow $6° < \theta < 7.5°$ range for which the (2 × 1) reconstruction is geometrically hindered. Thus, changes in the substrate surface structure affect the stability of SK islands, providing an explanation for the long-standing question of whether {1 0 5} faceting has a unique pathway in Ge/Si epitaxy. In addition, terraces formed on{1 0 5}-vicinal surfaces are wide enough to allow an optical study of their electronic properties [84].

3.3. Effect of the elastic field symmetry on the arrangements of self-assembled Ge nanostructures

By changing the miscut angle it is possible to tune the elastic-interaction potential among islands and therefore to study how the specific island's shape depends on the elastic interaction across a variety of realistic configurations of strain fields [66, 85]. The resulting effect that affects the island size depends on the elastic field intensity. For small islands, such as pyramids and ripples, the breaking of the elastic field symmetry induced by vicinality alters the lateral spatial ordering between islands. By contrast for large volume islands such as multifaceted domes, the elastic field drives the Ge growth through pathways different from those that arise in the case of Ge growth on planar silicon substrates.

Vicinal islands interact repulsively through their reciprocal strain fields in the surface [86–88]. We can define the mutual interaction energy Y as the extra energy density needed to create an island in a specific site when another island exists nearby:

$$\mathrm{Y} = U(\boldsymbol{r}) - U(\infty), \tag{27}$$

where $U(r)$ is the total energy strain density stored in the island and in the substrate for a pair of islands with relative distance r.

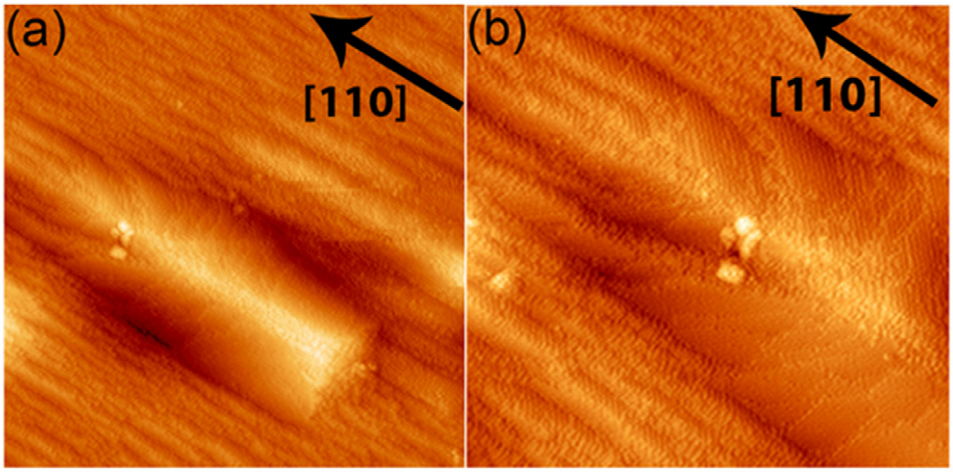

Figure 27. STM images of Ge ripples grown on the 8°-miscut Si(0 0 1) surface. Note that, due to the geometric constraint of vicinality, the down side of the ripple (b) is not bounded by {1 0 5} facets. Copyright Wiley-VCH Verlag GmbH & Co. Reproduced with permission [11].

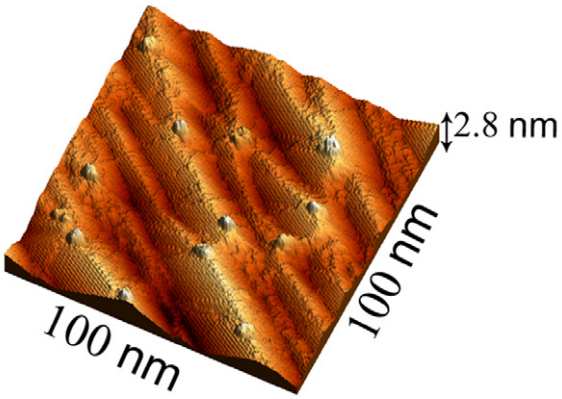

Figure 28. 3D STM image of the 8.05°-miscut Si(0 0 1) surface being completely covered with Ge ripples. Copyright Wiley-VCH Verlag GmbH & Co. Reproduced with permission [11].

The elastic interaction energy, calculated by FE, is almost isotropic for the two main configurations of a Ge island pair grown on a flat Si(0 0 1) surface (figure 36(a)). The situation is very different when the Ge island is grown on vicinal substrates which show a strong directional dependence of the elastic interactions, such dependence increasing for larger miscut angles (figure 36(b,c)). In this latter case the lowest-energy configuration corresponds to an islands pair aligned along the [1 1 0] miscut direction. The energy density maps of an island pair for miscut angles respectively of 6° (figure 36(d)) and 8° (figure 36(e)) display the elastic relaxation within and on the substrate around them by using two different scales. It is evident that at high vicinal angles the morphological anisotropy of islands breaks the symmetry of elastic potential producing directions of reduced interaction energy. It is worth noting that for large islands the specific shape of island is immaterial and the elastic interaction scales as in the case of two distributions of dipoles, i.e. as r^{-3} [86] (dotted curve in figure 36(a)). On the other hand at smaller distances the point-island approximation is no longer valid and the specific details of elastic energy depend on the island's shape. In summary, for small volume islands (e.g. pyramids and ripples) at an increasing miscut angle, the anisotropy of strain fields increases inside and around each island: This affects the short range local lateral arrangement of islands which becomes anisotropic [85].

In the case of Ge domes the elastic interactions are more intense but, nonetheless, they can also be tuned by substrate vicinality. In figure 37 the island's interaction energy and the correspondent contour plot are reported, respectively, for Ge domes grown on a flat (figure 37 (a) and (b)) and on 10°-miscut (figure 37(c) and (d)) Si(0 0 1) surface. In the case of a singular substrate the interaction potential reflects the four-fold symmetry and the islands' coalescence along the minima in the ⟨0 0 1⟩ directions. Conversely, for domes grown on vicinal substrates the breaking of island's symmetry produces directions with low elastic repulsion along which islands can come into contact. Soft configurations are obtained for islands interacting within an angular window of ±60° about the [1 1 0] direction (figure 37(d)). So the shape of elastic potential affects the impingement directions: This result is confirmed by the STM images measured in the case of Ge domes grown on 8° and 10°-miscut Si(0 0 1) substrates [66]. The statistical analysis on the distribution of impingement directions reported in figure 37(e, f) shows that the number of impingements is impressively larger along the elastically soft directions around[1 1 0]. This result proves experimentally that the elastic interaction anisotropy can be used to drive the pathways of Ge heteroepitaxy so providing new self-assembled strategies. Moreover this analysis can be applied to other hetereopitaxial systems for which elastic field is a common key parameter.

3.4. Size-dependent reversal of the elastic interaction energy

In the following we will show how the elastic interactions, that depend on the island shape, can deviate from the point-dipole approximation [86], changing drastically the interaction energy among islands and driving particular pathways in the ordering of islands. The specific shape of the elastic strain around and below the islands can modify the interactions usually experienced by equally sized islands from repulsive to attractive. In the framework of FE method we consider two

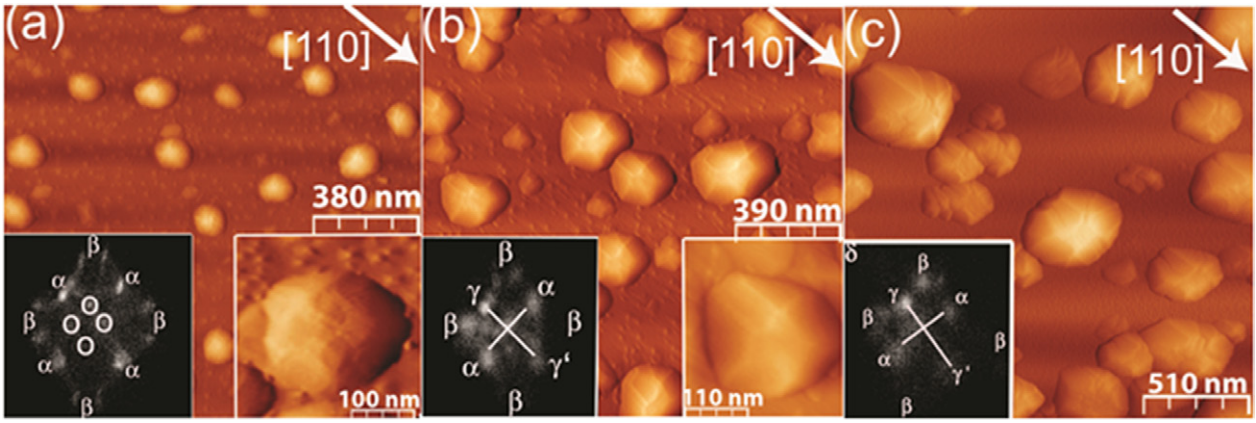

Figure 29. Morphology of Ge domes: (a) on the singular, (b) on the 8°-miscut and (c) on the 10°-miscut Si(0 0 1) surface. In the insets, the corresponding FPs are shown. The spots of the different facets are labeled as follows: {1 0 5} by ◯; {1 1 3} by α; {15 3 23} by β; {1 1 1} by δ; the new facets along the miscut direction on vicinal substrates are indicated by γ and $\gamma\prime$. Copyright Wiley-VCH Verlag GmbH & Co. Reproduced with permission [11].

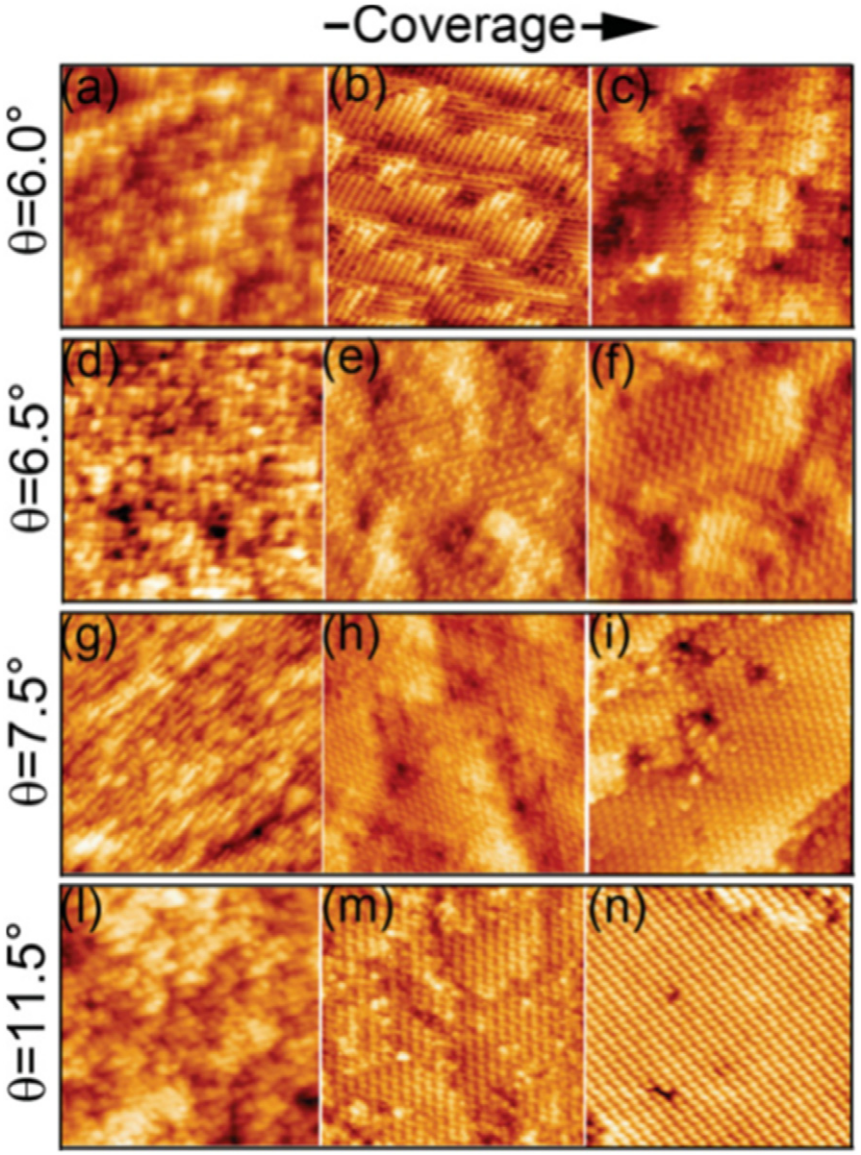

Figure 30. STM images, (24 × 24) nm^2, showing the strain-induced structural evolution of vicinal Si(0 0 1) surfaces at increasing Ge coverage: (a, d, g, l) clean surfaces; (b, e, h, m) 0.4 ML of Ge; (c, f, i, n) 1.3 ML of Ge. Image (n) has positive sample bias. θ is the misorientation angle from the (0 0 1) face toward the [1 0 0] direction. In the images, the horizontal and vertical axes are oriented along the ⟨1 1 0⟩ directions. Copyright American Physical Society. Reproduced with permission from [109].

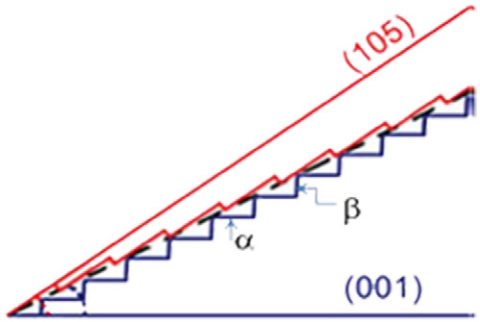

Figure 31. The alternative step structures of a vicinal (0 0 1) and (1 0 5) surface. The terrace and step edge surface energies are labeled α and β, respectively. Copyright American Physical Society. Reproduced with permission from [109].

nanostructures elastically interacting on a half space namely a (1 1 1) surface of Si: a large island and a small neighboring cluster (figure 38). A rotational symmetry has been taken into account, assuming a large island with cylindrical shape and an aspect ratio equal to 0.1 and a small hemispherical cluster with variable size and position.

The interaction energy Y is calculated for different values of the ratio between the cluster (R_c) and island (R_i) radius. In figure 39(a, b) the elastic energy surface of an island-cluster pair with R_c/R_i ratio equal to 0.25 and 0.0125 respectively is reported. It is evident that for largest cluster radius the interaction energy is positive everywhere leading to a repulsive interaction tending to disadvantage the formation of a cluster close to the island. Conversely, when the cluster size is reduced, the interaction potential changes drastically, assuming a potential well shape and showing that clustering lowers the total strain energy of the system. To identify the physical origin of such an attractive interaction we have analyzed the detailed shape of elastic field for a single island-cluster pair, as displayed in figure 40, where the strain is mapped on the side of the island close to the cluster and on the opposite side. The cluster generates a dual effect: on the one hand it produces a relaxation of the compressive strain generated from the island; on the other hand is itself a source of compression that depends on its size. The total effect can lower or increase the total energy of the system. To take into account the relative weight of these two contributions the in-plain strain integral, $\int_0^x |\varepsilon_\parallel(x')|\,\mathrm{d}x'$, along the substrate surface is reported as a function of $x = r_x/R_i$ on the side of the island close to the cluster and on the opposite side. If we compare the results in the case of a small cluster (figure 40(a) and (b)) the total strain appears flat under the cluster; this shows that in this position the strain is partially relieved and the total energy is lower than that on the cluster free side. Conversely, for the large cluster, (figure 40(c) and (d)), the in-plane strain integral is no longer flat under the cluster while outside the cluster edge the compression is clearly evident. In the case of $R_c/R_i = 0.0125$, if we consider the cooperative contribution of several independent clusters, we obtain the results shown in figure 41 in which it is evident that the more numerous are the islands, the deeper is the interaction energy well.

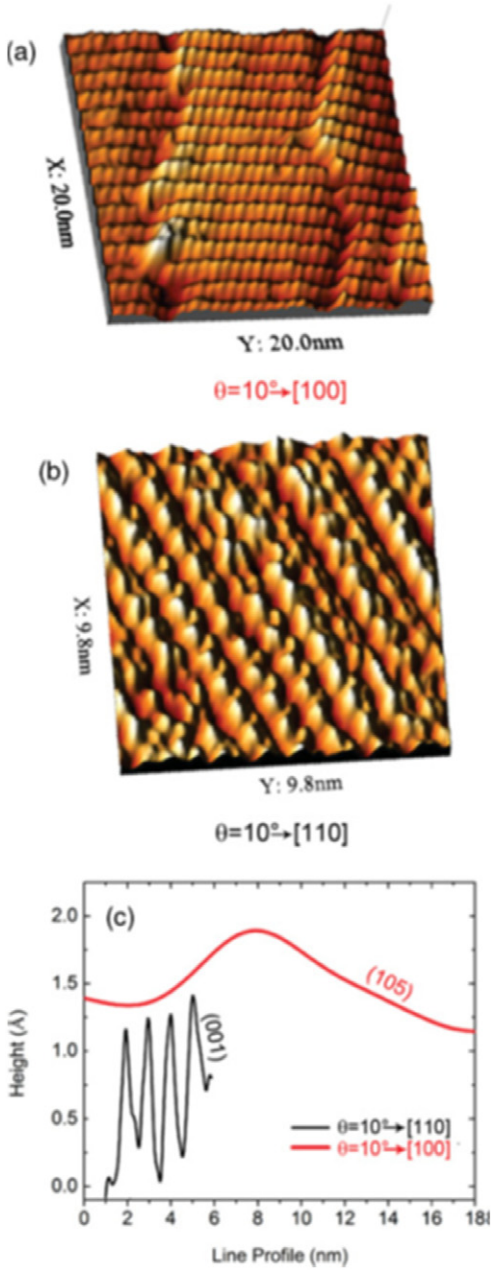

Figure 32. STM images of a vicinal (1 0 5) surface (a) and a vicinal (0 0 1) surface (b) at a polar angle of $\theta = 10^\circ$ and azimuthal misorientation toward the [1 1 0] and the [1 0 0] directions, respectively. The vicinal (1 0 5) surface has markedly larger terraces, as evident from the corresponding line profiles shown in panel (c). Copyright American Physical Society. Reproduced with permission from [109].

In other words the island attracts many clusters around it. This theoretical prediction is confirmed by the experiment [110] shown in figure 42. Around a large island, grown by depositing 10 ML of Ge at 873 K on a Si(1 1 1) substrate, a trench region where several clusters nucleate is apparent. Their density is not homogeneous this being higher in close proximity to the island edge. Moreover the trenches visually trace out the compressive region around the island edges [24] which attract the clusters as is predicted by the simulations.

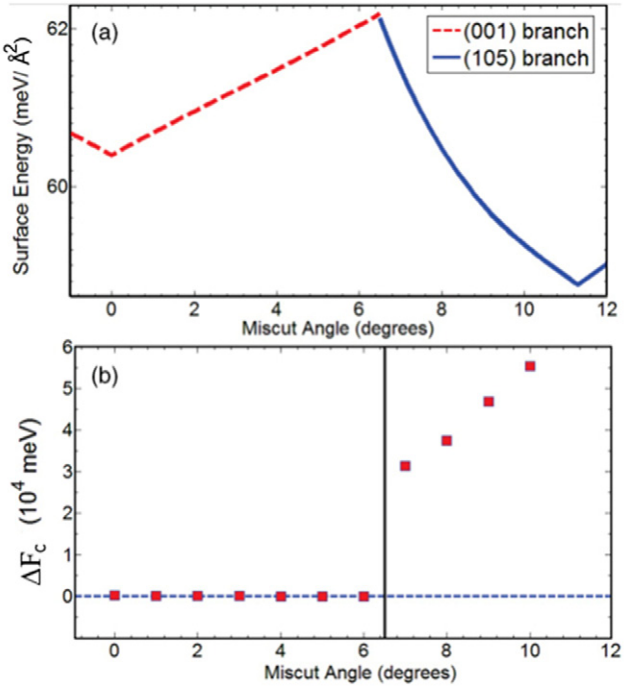

Figure 33. (a) σ-plot of strained Si between the (0 0 1) and the (1 0 5) orientations. (b) Activation energy for $\{1\,0\,5\}$ islanding as a function of the miscut polar angle.]. Copyright American Physical Society. Reproduced with permission from [109].

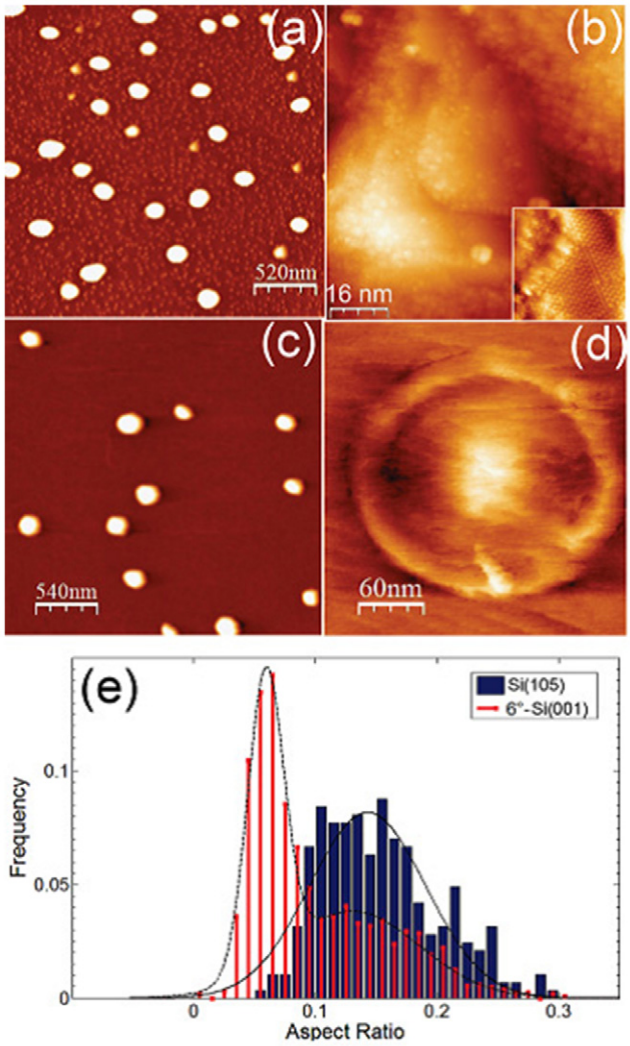

Figure 34. (a, b) STM images of the 6°-miscut Si(0 0 1) surface. (a) Bimodal island distribution at a coverage of 5.5 ML of Ge. (b) Snapshot of a skewed pyramid bounded by $\{1\,0\,5\}$ facets. In the inset, (20×20) nm^2, the RS reconstruction of the facets is evident.(c, d) STM images of the 7.5°-miscut Si(0 0 1) surface. (c) Unimodal distribution of domes at a coverage of 5.5 ML of Ge. (d) Precursor of domes growing from the planar WL. (e) Distribution of the island aspect ratio on a 6°-miscut Si(0 0 1) surface and a Si(1 0 5) surface. The two distributions are fitted to Gaussian functions. Copyright American Physical Society. Reproduced with permission from [109].

4. The effect of intermixing on elastic relaxation

In this section, we will discuss some important issues which have been neglected in the previous description of elastic relaxation. If we re-examine equation (23), we could ask, e.g. what specific surface energy, σ, has been used—as done—for the free energy. From section 2, we know that σ of a strained epilayer is an unknown function of its thickness which must be calculated numerically. It has been shown [89], however, that this dependence can be well approximated by a quasi-exponential decrease of σ with thickness d

$$\sigma(d) = \sigma_{\text{sub}}^{\infty} + \left(\sigma_{\text{WL}}^{\infty} - \sigma_{\text{sub}}^{\infty}\right)\left(1 - \mathrm{e}^{-d/\eta}\right). \qquad (28)$$

For Ge/Si, equation (28) fits nicely the *ab initio* data for $\eta = 1$. Obviously, the correction is mostly effective at low thickness ($d < 2$ ML), where the surface energy drops from the value of the bare Si towards that of the bulk Ge. At larger coverage, i.e. for WL thickness between 3 and 4 ML at which nucleation of 3D islands occurs [24], one can safely use the surface energy density of a strained infinite Ge layer without altering significantly the total free energy gain.

It is much more important to take into account the substrate-deposit alloying, since intermixing can drastically reduce the misfit parameter and the latter has a quadratic dependence on the volume strain energy density. This means that a drop in the lattice mismatch causes a substantial fall of the strain energy density. In the case of Ge/Si, a $Si_{1-x}Ge_x$ random alloy of average lattice mismatch $f(x) = 0.04x$ and average composition x close to 0.50 [62, 90, 91] is formed. Direct evidence of intermixing is, e.g. the appearance of buckled Ge dimer sites on the Si(0 0 1) WL [92, 93] and of trenches surrounding the islands [60, 62].

Experiments show that the equilibrium shape of the islands is not excessively changed by intermixing at the typical temperatures used in growth experiments [94]. This allows us to treat alloying as a correction to the equilibrium shape predicted by the elastic FE analysis applied to unalloyed islands. Let us assume, as a first approximation, that alloying in the island is uniform. According to the Vegard's law, the elastic constants of the alloy are then linearly interpolated between Si

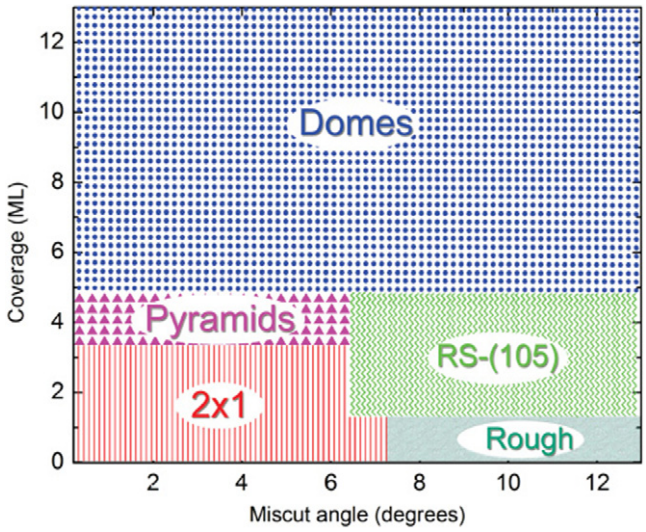

Figure 35. Schematic orientational experimental phase diagram of Si/Ge surface vicinal to the (0 0 1) and the (1 0 5) planes along the [1 0 0] direction, as a function of Ge coverage. The sharp boundaries are for guidance only. Copyright American Physical Society. Reproduced with permission from [109].

and Ge ones, namely

$$C_{ij}(x) = C_{ij}^{\mathrm{Ge}} x + C_{ij}^{\mathrm{Si}} (1 - x)\,, \tag{29}$$

where C_{ij}^{Ge} and C_{ij}^{Si} are the stiffness tensors of pure Ge and Si, respectively (table 1). We can therefore perform FE simulations of elastic relaxation of $Si_{1-x}Ge_x$ islands as a function the Ge composition x and, for each island, compute the relaxation factor $R(r,x)$, by comparing the elastic energy density to that of a $Si_{1-x}Ge_x$ strained film of the same composition which reads (figure 43)

$$\rho_{\mathrm{WL}}(x) = \left\{C_{11}(x) + C_{12}(x) - 2[C_{12}(x)]^2/C_{11}(x)\right\}[f(x)]^2\,. \tag{30}$$

Figure 44 shows that the scaling with the aspect ratio is only slightly dependent on the island's composition. The behavior can still nicely be fitted by an exponential form $R(r, x) = \mathrm{e}^{-k(x)r}$ [45] in which the decay constant $k(x)$ shows a weak linear dependence on Ge composition (figure 45). The decrease of the decay constant with Ge content is due to the smaller elastic constants of Ge compared to Si. Introducing the composition-dependence in equation (20), one can predict the preferential aspect ratio for each volume, i.e. the island's shape evolution, as a function of the alloying content (figure 46). Since alloying cooperates/competes with shape change for elastic relaxation [6, 95], the results obtained are clear: for intermixed islands, the evolution towards steeper morphology is shifted to larger critical volumes.

As evident from figure 18, strain energy is not completely relieved for pure Ge islands, but remains concentrated at the bottom edges of the islands. Elastic relaxation mediated by alloying is instead more efficient, thanks to the injection of Si atoms from the substrate. Moreover, by plotting the relative difference of relaxation factors $\Delta R/R$ between shallow ($r = 0.05$) and steep islands ($r = 0.7$) for different Ge content (figure 47), one can also notice that the free-energy gap between shallow and steep islands is broadened by Ge redistribution [96].

Despite the assumption of uniform alloying being a good starting point for our analysis, it is not fully consistent with experimental results which reveal, instead, relatively non-homogeneous concentration profiles. The alloying distribution inside the islands can be probed by scattering experiments, such as anomalous x-ray diffraction [94, 97]. The results suggest an increase of the average Ge content moving from the base toward the top. For instance, Wiebach *et al* [98] report Ge concentrations of 25% in the lower and 30% in the upper part at about one third of the island height, while Malachias *et al* [94] find a Si-rich core covered by a Ge-rich external shell.

Both thermodynamic and/or kinetic driving forces have been suggested for alloying and the literature on the subject is worth of a review paper in itself (see, e.g. [99]). Nonetheless, predicting at the same time both the equilibrium shape and composition of the dots remains a challenging task. We will consider here a very instructive model proposed by Spencer and Blanariu [100] in which the concentration $c(r, z)$ and the dot shape $h(r)$ are calculated in close form for a Ge island on Si(0 0 1) in the small-island limit. This is only possible within the approximation of negligible bulk diffusion and rather fast surface diffusion. One starts from the constitutive equations (16) and includes, in the diagonal components of the strain tensor ε_{ij}, a compositional strain $-\eta[c(r, z) - c_0]$, this being proportional to the expansion coefficient η of Ge within the WL film and zero in the Si substrate. c_0 is the average composition of the island of volume V. The chemical potentials $\mu_i = \mathrm{d}G_i/\mathrm{d}c$, which are defined for each atomic species (i = Ge and Si), depend on the elastic strain and composition. A fully miscible random alloy is assumed [101]. As the island shape is computed self-consistently using equation (15), the non-uniform stress field results in a non-uniform composition along the surface. For small island volume and low aspect ratio, the equilibrium $h(r)$ and $c(r, z)$ profiles can be disentangled, giving

$$h(r) = A\left[a_0 + \sum_{j=1}^{\infty} a_j J_0\left(\frac{z_j r}{R}\right)\right], \tag{31}$$

and

$$c(r, z) = C\left[\alpha + \frac{L}{r}\frac{\mathrm{d}}{\mathrm{d}r}\left(r\frac{\mathrm{d}h(r)}{\mathrm{d}r}\right)\right]\frac{z}{h(r)}, \tag{32}$$

where J_0 is the zeroth order Bessel function and z_j is the jth zero of $J_1(z)$. L is a length scale factor and C sets the amount of strain-induced segregation which increases with the lattice misfit $\varepsilon = -\eta x$. Figure 48 shows concentration profiles obtained, as the island grows, from the burial of successive layers with variable composition. In a very good match with

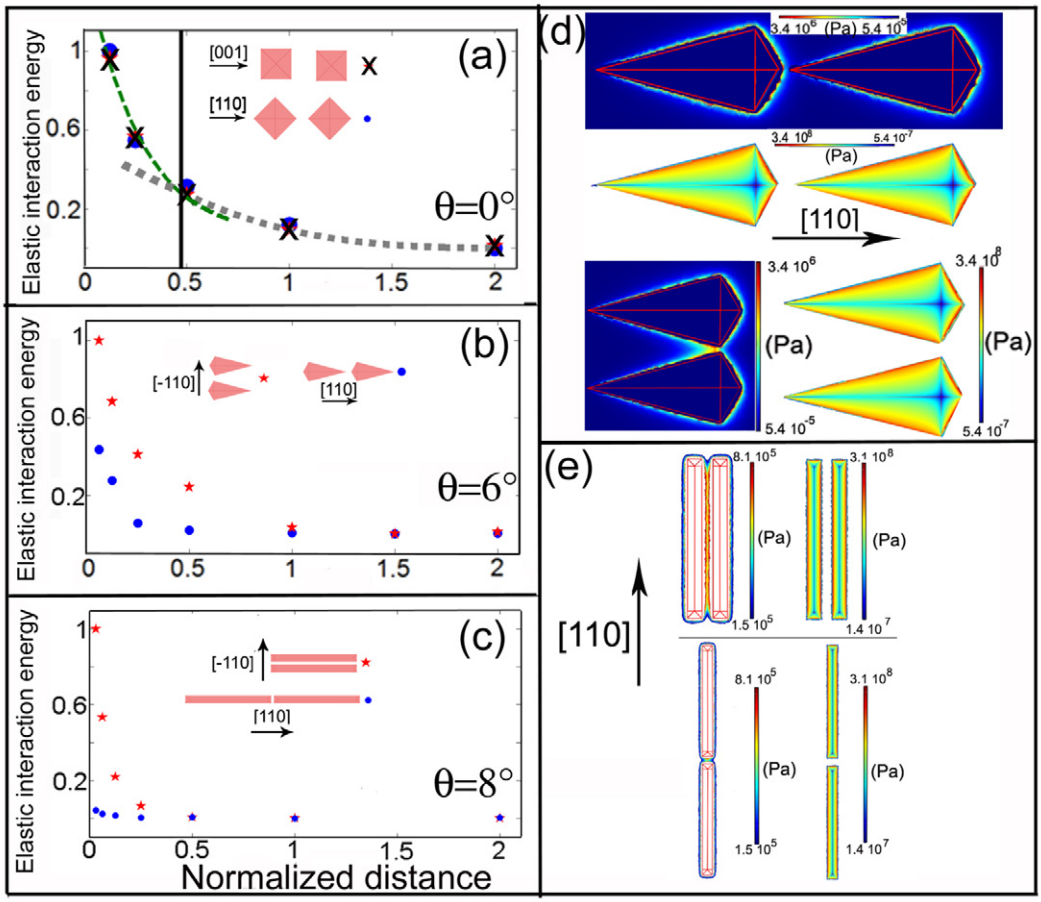

Figure 36. (a–c) Elastic interaction energy for different configurations of an island pair (a) on the singular, (b) on the 6°-miscut, and (c) on the 8°-miscut Si(0 0 1) surfaces (vertical axis in arbitrary units, horizontal axis in units of the average island side). The data in the panel (a) are fitted to a r^{-3} function at large island separations (dotted curve) and to an exponential function at short separations (dashed curve). The vertical line marks the boundary between the two regimes. Elastic energy density maps of an island pair on (d) 6°-miscut and (e) 8°-miscut surfaces. Each plot is displayed with two different scales giving the elastic relaxation within the islands and on the substrate around them. Copyright American Physical Society. Reproduced with permission [85].

experimental observation, the composition map indicates that Ge tends to segregate close to the apex of the island where the elastic strain is minimum. Nonetheless, the model is not able to describe features, such as Si enrichment around the corners of faceted islands, which suggest relevant kinetic restrictions, completely neglected in this picture [102, 103].

In principle, Monte Carlo (MC) simulations are able to obtain concentration profiles minimizing the system free energy of the system [31, 104, 105] by using an iterative procedure consisting of chemical-species random exchange, energy optimization and acceptance probability determined by Boltzmann statistical weights. Once again, the application of this approach is somehow limited by the demanding computational cost when treating islands with realistic size/shape. One could think of circumventing this issue with scaling-down approaches, but then face the problem of reproducing facets with a minimum physically meaningful extension [96]. A possible solution would be combining MC-FE methods for a fast self-consistent calculation of SiGe distribution minimizing the elastic energy [96, 106]. In practice, an additional mesh defines a non-uniform composition grid. The values assigned to the latter are randomly changed (maintaining constant the average composition) by an iterative procedure with an acceptance criterion based on the minimization of elastic energy at each step by FE calculations. It is clear that the alloying distribution obtained is dictated by thermodynamics alone. Therefore, the iso-composition maps match those obtained by selective wet chemical etching [103] only for moderate growth temperature ($T \sim 580\,^{\circ}\mathrm{C}$). Conversely, for islands grown at higher temperature at which kinetic effects cannot be neglected, the experimental composition profiles are much more uniform than the simulated ones [96]. The ultimate goal is therefore to develop methods assessing both kinetics and thermodynamics. At present initial attempts have been limited to simplified 2D models [107], albeit they could explain qualitatively some experimental findings of the heteroepitaxial growth.

5. Summary

Through a critical analysis of a number of experimental and theoretical aspects concerning Ge on Si growth, we have

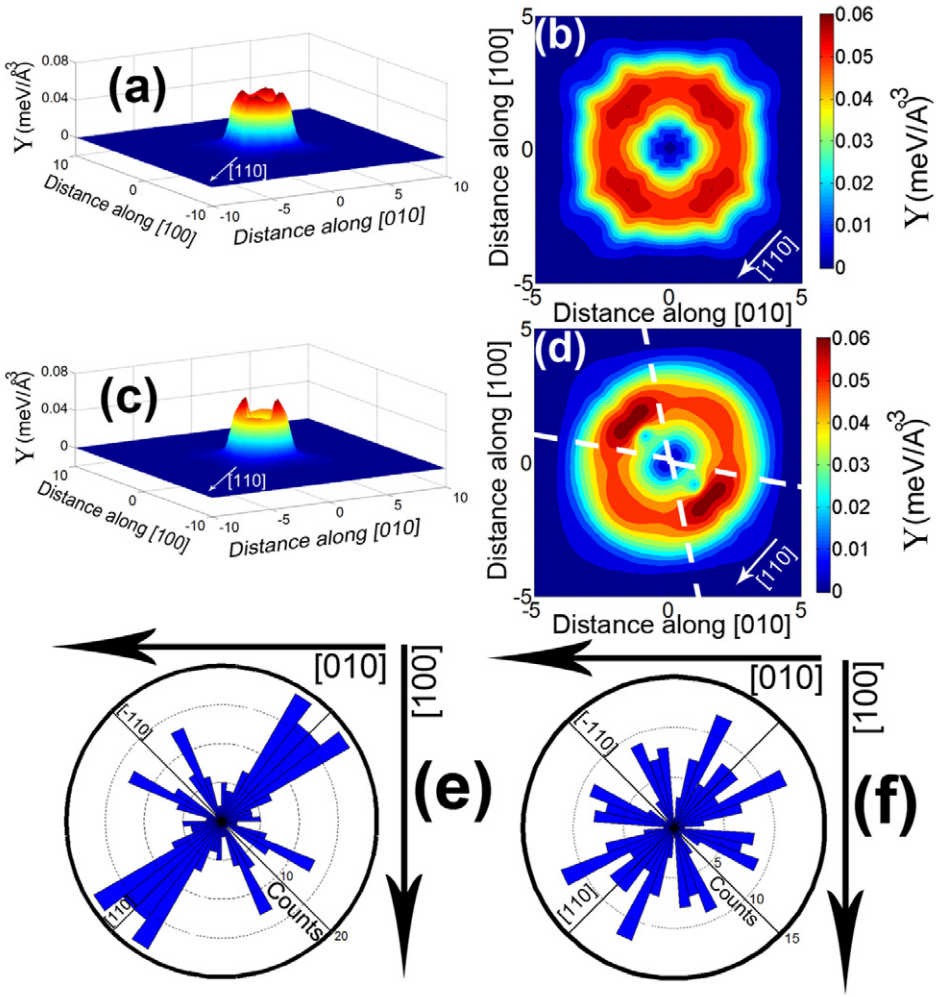

Figure 37. (a) Interaction energy surface of Ge domes on the singular Si(0 0 1) surface and (b) corresponding contour plot. (c) Interaction energy surface of Ge domes on 10°-miscut Si(0 0 1) surface and (d) corresponding contour plot (The region of reduced interaction energy around the miscut direction is highlighted). Angular distribution of impingement directions measured (e) on 8°-miscut Si(0 0 1) substrates and (f) on 10°-miscut Si(0 0 1) substrates. Copyright American Physical Society. Reproduced with permission [66].

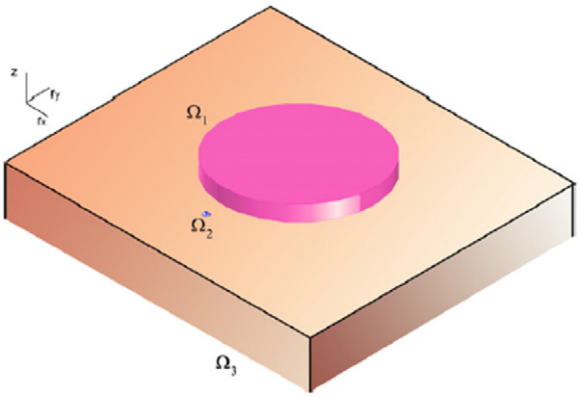

Figure 38. The geometric model used in the FE simulations. The system consists of a large Ge island interacting with a small Ge (Ω_1) cluster (Ω_2) through a Si substrate (Ω_3). Copyright IOP Science. Reproduced with permission [110].

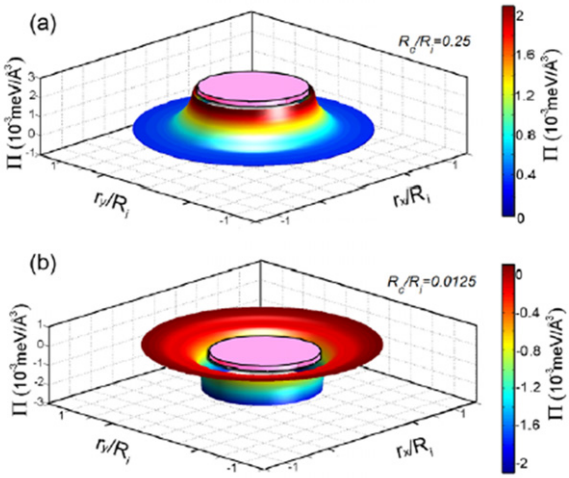

Figure 39. The elastic interaction energy surface of a Ge island interacting with a cluster for (a) $R_c/R_i = 0.25$ and (b) $R_c/R_i = 0.0125$. The scale of the horizontal axis is given in units of the radius of the island. The geometric boundary of the island is highlighted. Copyright IOP Science. Reproduced with permission [110].

examined the pivotal role of elasticity in strained epitaxial systems. The problem of stability of QD morphology has

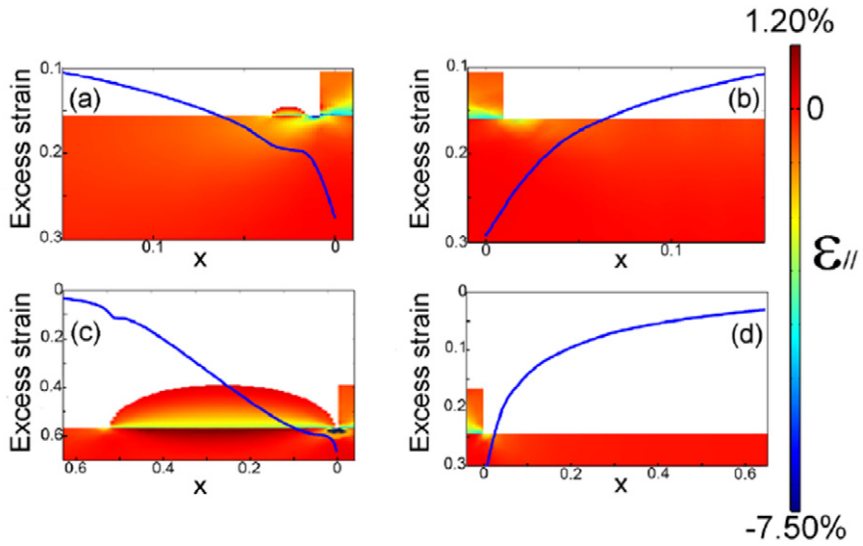

Figure 40. The in-plane strain distribution in the interacting island–cluster system for $R_c/R_i = 0.0125$ (panels (a) and (b)) and $R_c/R_i = 0.25$ (panels (c) and (d)). For the two values of the size parameter, the strain is mapped on the side of the island close to the cluster and on the opposite side. The spatial dependence, as a function of $x = r_x/R_i$, of the path integral of $\varepsilon_{\parallel}$ along the substrate surface is superimposed on the strain IOP Science maps. Copyright. Reproduced with permission [110].

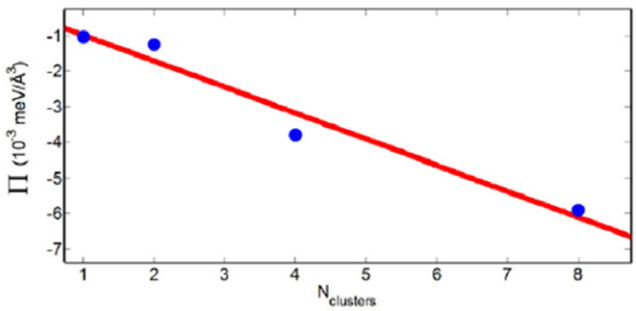

Figure 41. The depth of the interaction energy well as a function of the number of clusters for $R_c/R_i = 0.0125$. The continuous line is a linear fit to the data. Copyright IOP Science. Reproduced with permission [110].

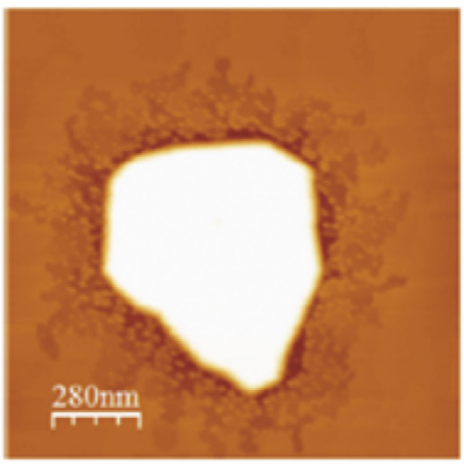

Figure 42. STM images of large Ge island surrounded by clusters on a Si(1 1 1) surface at a Ge coverage of 10 ML. Adapted from [110].

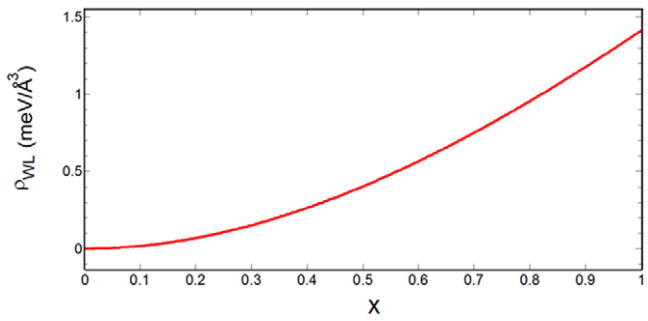

Figure 43. Elastic energy density of a flat $Si_{1-x}Ge_x$ epilayer grown on Si as a function of the Ge content.

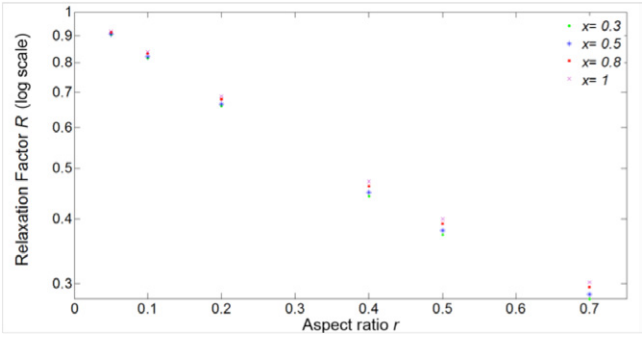

Figure 44. Relaxation factor versus aspect ratio for $Si_{1-x}Ge_x$ pyramids of different Ge content. Copyright Wiley-VCH Verlag GmbH & Co. Reproduced with permission [11].

been examined in the framework of continuum elasticity theory and useful analytical formulas applicable to simple morphologies are provided. The results of modeling have been compared with the experimental STM data taken on

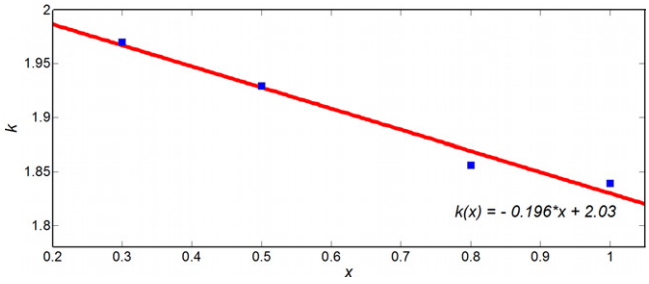

Figure 45. Dependence of the decay constant $k(x)$ on the Ge content x in the alloy. Copyright Wiley-VCH Verlag GmbH & Co. Reproduced with permission [11].

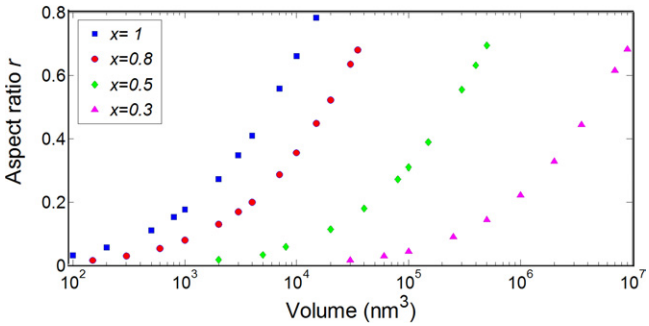

Figure 46. Thermodynamically favored aspect ratio of $Si_{1-x}Ge_x$ islands as a function of volume obtained by FE simulations. Copyright Wiley-VCH Verlag GmbH & Co. Reproduced with permission [11].

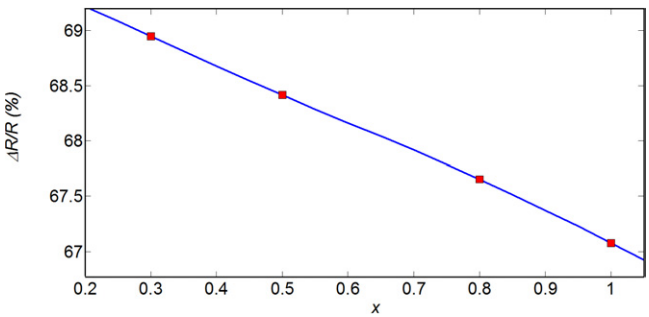

Figure 47. Relative difference of relaxation factors between shallow ($r = 0.05$) and steep ($r = 0.7$) $Si_{1-x}Ge_x$ islands as a function the Ge content in the alloy. Copyright Wiley-VCH Verlag GmbH & Co. Reproduced with permission [11].

SiGe as a function of coverage to assess the validity of model descriptions against realistic growths. In this context, we have assessed several case studies in which the anisotropy of the elastic interactions, induced by substrate symmetry- as crystallographic orientation, steps, and vicinality- crucially determines the growth behavior. The issue of strain-biased diffusion has also been briefly discussed. Finally, we have addressed the problem of intermixing starting from homogeneous alloying and then shifting to more realistic compositional maps.

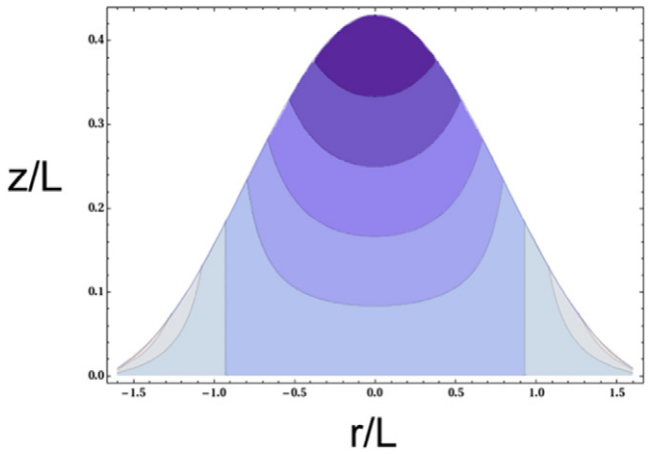

Figure 48. Island shape and composition map according to equation (32). The lateral size of the island is L. The composition map is a contour plot of the composition profile $c(r, z)/C$, the scaled deviation from a reference composition C. The step between contours is 0.25, vertical lines are the zero contours, and dark corresponds to the larger misfit component (i.e. Ge). Copyright Wiley-VCH Verlag GmbH & Co. Reproduced with permission [11].

Acknowledgments

LP acknowledges the support from the ETH Zurich Postdoctoral Fellowship Program and the Marie Curie Actions for People COFUND Program.

References

[1] Mo Y W, Savage D E, Swartzentruber B S and Lagally M G 1990 *Phys. Rev. Lett.* **65** 1020
[2] Eaglesham D J and Cerullo M 1990 *Phys. Rev. Lett.* **64** 1943
[3] Scappucci G, Capellini G, Klesse W M and Simmons M Y 2013 *Nanoscale* **5** 2600
[4] Zwanenburg F A, Dzurak A S, Morello A, Simmons M Y, Hollenberg L C L, Klimeck G, Rogge S, Coppersmith S N and Eriksson M A 2013 *Rev. Mod. Phys.* **85** 961
[5] Aqua J N, Berbezier I, Favre L, Frisch T and Ronda A 2013 *Phys. Rep.* **522** 59
[6] Berbezier I and Ronda A 2009 *Surf. Sci. Rep.* **64** 47
[7] Stangl J, Holý V and Bauer G 2004 *Rev. Mod. Phys.* **76** 725
[8] Voigtländer B 2001 *Surf. Sci. Rep.* **43** 127
[9] Royer L 1928 *Bull. Soc. Fr. Mineral.* **51** 7
[10] Rumyantsev S and Shur M 1996 *Handbook Series on Semiconductor Parameters* vol 2 (London: World Scientific)
[11] Sgarlata A, Persichetti L and Balzarotti A 2014 *Surface and Interface Science* vol 4, ed K Wandelt (New York: Wiley) p 863
[12] Pang Y and Huang R 2009 *Int. J. Solids Struct.* **46** 2822
[13] Politi P, Grenet G, Marty A, Ponchet A and Villain J 2000 *Phys. Rep.* **324** 271
[14] Tersoff J and LeGoues F K 1994 *Phys. Rev. Lett.* **72** 3570
[15] Tersoff J and Tromp R M 1993 *Phys. Rev. Lett.* **70** 2782
[16] Brehm M *et al* 2009 *Phys. Rev.* B **80** 205321
[17] Lu G and Liu F 2005 *Phys. Rev. Lett.* **94** 176103
[18] Lu G, Cuma M and Liu F 2005 *Phys. Rev.* B **72** 125415
[19] Tu Y and Tersoff J 2004 *Phys. Rev. Lett.* **93** 2216101
[20] Li X L, Ouyang G and Yang G W 2007 *Phys. Rev.* B **75** 245428
[21] Sutter P and Lagally M G 2000 *Phys. Rev. Lett.* **84** 4637
[22] Tromp R M, Ross F M and Reuter M C 2000 *Phys. Rev. Lett.* **84** 4641

[23] Goldfarb I 2005 *Phys. Rev. Lett.* **95** 025501
[24] Szkutnik P D, Sgarlata A, Nufris S, Motta N and Balzarotti A 2004 *Phys. Rev.* B **69** 201309
[25] Tersoff J, Spencer B J, Rastelli A and von Känel H 2002 *Phys. Rev. Lett.* **89** 196104
[26] Vailionis A, Cho B, Glass G, Desjardins P, Cahill D and Greene J E 2000 *Phys. Rev. Lett.* **85** 3672
[27] Hopcroft M A, Nix W D and Kenny T W 2010 *J. Microelectromech. Syst.* **19** 229
[28] Landau L D 1959 *Theory of Elasticity* (Oxford: Pergamon)
[29] Shchukin V and Bimberg D 1999 *Rev. Mod. Phys.* **71** 1125
[30] Zinovyev V A, Vastola G, Montalenti F and Miglio L 2006 *Surf. Sci.* **600** 4777
[31] Sonnet P and Kelires P C 2004 *Appl. Phys. Lett.* **85** 203
[32] Martinelli L, Marzegalli A, Raiteri P, Bollani M, Montalenti F, Miglio L, Chrastina D, Isella G and von Känel H 2004 *Appl. Phys. Lett.* **84** 2895
[33] Raiteri P, Migas D B, Miglio L, Rastelli A and von Känel H 2002 *Phys. Rev. Lett.* **88** 256103
[34] Tersoff J, Teichert C and Lagally M G 1996 *Phys. Rev. Lett.* **76** 1675
[35] Makeev M and Madhukar A 2001 *Phys. Rev. Lett.* **86** 5542
[36] Marchetti R, Montalenti F, Miglio L, Capellini G, De Seta M and Evangelisti F 2005 *Appl. Phys. Lett.* **87** 261919
[37] Retford C M, Asta M, Miksis M J, Voorhees P W and Webb E B 2007 *Phys. Rev.* B **75** 075311
[38] Vastola G, Gatti R, Marzegalli A, Montalenti F and Miglio L 2008 *Self-Assembled Quantum Dots* ed Z Wang (New York: Springer) p 421
[39] Kratzer P, Liu Q K K, Diaz A, Manzano C, Costantini G, Songmuang R, Rastelli A, Schmidt O G and Kern K 2006 *Phys. Rev.* B **73** 205347
[40] Jonsdottir F 2006 *Modelling Simul. Mater. Sci. Eng.* **14** 1167
[41] Pryor C, Kim J, Wang L W, Williamson A J and Zunger A 1998 *J. Appl. Phys.* **83** 2548
[42] Zhou W, Cai C, Yin S and Wang C 2008 *Appl. Surf. Sci.* **255** 2400
[43] Eshelby J D 1957 *Proc. R. Soc.* A **241** 376
[44] Muller P and Saul A 2004 *Surf. Sci. Rep.* **54** 157
[45] Gatti R, Pezzoli F, Boioli F, Montalenti F and Miglio L 2012 *J. Phys.: Condens. Matter* **24** 104018
[46] Rastelli A and von Känel H 2002 *Surf. Sci.* **515** L493
[47] Fujikawa Y, Akiyama K, Nagao T, Sakurai T, Lagally M G, Hashimoto T, Morikawa Y and Terakura K 2002 *Phys. Rev. Lett.* **88** 176101
[48] Migas D B, Cereda S, Montalenti F and Miglio L 2004 *Surf. Sci.* **556** 121
[49] Cereda S, Montalenti F and Miglio L 2005 *Surf. Sci.* **591** 23
[50] Medeiros-Ribeiro G, Bratkovski A, Kamins T, Ohlberg D and Williams S 1998 *Science* **279** 353
[51] Ross F M, Tersoff J and Tromp R M 1998 *Phys. Rev. Lett.* **80** 984
[52] Montalenti F *et al* 2004 *Phys. Rev. Lett.* **93** 216102
[53] Sutter E, Sutter P and Bernard J E 2004 *Appl. Phys. Lett.* **84** 2262
[54] Stoffel M, Rastelli A, Tersoff J, Merdzhanova T and Schmidt O G 2006 *Phys. Rev.* B **74** 155326
[55] Brehm M, Lichtenberger H, Fromherz T and Springholz G 2011 *Nanoscale Res. Lett.* **6** 70
[56] Motta N, Sgarlata A, Rosei F, Szkutnik P D, Nufris S, Scarselli M and Balzarotti A 2003 *Mater. Sci. Eng.* B **101** 77
[57] Larché F C and Cahn 1982 *Acta Metall.* **30** 1835
[58] Larché F C and Cahn J W 1985 *Acta Metall.* **33** 331
[59] Barabási A 1997 *Appl. Phys. Lett.* **70** 2565
[60] Persichetti L, Sgarlata A, Fanfoni M and Balzarotti A 2013 *J. Phys.: Condens. Matter* **25** 395801
[61] Shklyaev A A and Ponomarev K E 2015 *J. Cryst. Growth* **413** 94
[62] Motta N, Boscherini F, Sgarlata A, Balzarotti A, Capellini G, Ratto F and Rosei F 2007 *Phys. Rev.* B **75** 035337
[63] Persichetti L, Sgarlata A, Fanfoni M, Bernardi M and Balzarotti A 2009 *Phys. Rev.* B **80** 075315
[64] Spencer B J and Tersoff J 2010 *Appl. Phys. Lett.* **96** 073114
[65] Persichetti L, Sgarlata A, Fanfoni M and Balzarotti A 2010 *Phys. Rev. Lett.* **104** 036104
[66] Persichetti L, Sgarlata A, Fanfoni M and Balzarotti A 2011 *Phys. Rev. Lett.* **106** 055503
[67] Nakaoka T, Kako S, Ishida S, Nishioka M and Arakawa Y 2002 *Appl. Phys. Lett.* **81** 3954
[68] Kumar J, Kapoor S, Gupta S and Sen P 2006 *Phys. Rev.* B **74** 115326
[69] Zhu J, Brunner K and Abstreiter G 1998 *Appl. Phys. Lett.* **72** 424
[70] Teichert C, Bean J C and Lagally M G 1998 *Appl. Phys.* A **67** 675
[71] Ronda A and Berbezier I 2004 *Physica* E **23** 370
[72] Sutter P, Sutter E and Vescan L 2005 *Appl. Phys. Lett.* **87** 161916
[73] Lichtenberger H, Mühlberger M and Schäffler F 2005 *Appl. Phys. Lett.* **86** 131919
[74] Szkutnik P D, Sgarlata A, Balzarotti A, Motta N, Ronda A and Berbezier I 2007 *Phys. Rev.* B **75** 033305
[75] Shenoy V B, Ciobanu C V and Freund L B 2002 *Appl. Phys. Lett.* **81** 364
[76] Zhang X, Yu Y, Sun X-H and Ren X 2014 *J. Appl. Phys.* **115** 163508
[77] Persichetti L, Sgarlata A, Fanfoni M and Balzarotti A 2013 *Thin Solid Films* **543** 88
[78] Lobanov D N, Novikov A V, Vostokov N V, Drozdov Y N, Yablonskiy A N, Krasilnik Z F, Stoffel M, Denker U and Schmidt O G 2005 *Opt. Mater.* **27** 818
[79] Zhou T and Zhong Z 2014 *APL Mater.* **2** 022108
[80] Persichetti L, Sgarlata A, Fanfoni M and Balzarotti A 2010 *Phys. Rev.* B **82** 121309
[81] Chen G, Wintersberger E, Vastola G, Groiss H, Stangl J, Jantsch W and Schäffler F 2010 *Appl. Phys. Lett.* **96** 103107
[82] Chen G, Sanduijav B, Matei D, Springholz G, Scopece D, Beck M J, Montalenti F and Miglio L 2012 *Phys. Rev. Lett.* **108** 055503
[83] Zhong Z, Gong H, Ma Y, Fan Y and Jiang Z 2011 *Nanoscale Res. Lett.* **6** 322
[84] Fazi L, Hogan C, Persichetti L, Goletti C, Palummo M, Sgarlata A and Balzarotti A 2013 *Phys. Rev.* B **88** 195312
[85] Persichetti L, Sgarlata A, Fanfoni M and Balzarotti A 2010 *Phys. Rev.* B **81** 113409
[86] Rickman J and Srolovitz D 1993 *Surf. Sci.* **284** 211
[87] Johnson H T and Freund L B 1997 *J. Appl. Phys.* **81** 6081
[88] Ramasubramaniam A and Shenoy V B 2004 *J. Appl. Phys.* **95** 7813
[89] Li X L and Yang G W 2008 *Appl. Phys. Lett.* **92** 171902
[90] Drucker J 2002 *IEEE J. Quantum Electron.* **38** 975
[91] Boscherini F, Capellini G, Di Gaspare L, Rosei F, Motta N and Mobilio S 2000 *Appl. Phys. Lett.* **76** 682
[92] Qin X R, Swartzentruber B S and Lagally M G 2000 *Phys. Rev. Lett.* **84** 4645
[93] Zhou T, Renaud G, Revenant C, Issartel J, Schulli T U, Felici R and Malachias A 2011 *Phys. Rev.* B **83** 195426
[94] Malachias A, Kycia S, Ribeiro M, Magalh aes P, Kamins T I and Williams S 2003 *Phys. Rev. Lett.* **91** 176101
[95] Shiraki Y and Usami N S 2011 *Silicon–Germanium (SiGe) Nanostructures: Production, Properties and Applications in Electronics* (Sawston: Woodhead)
[96] Digiuni D, Gatti R and Montalenti F 2009 *Phys. Rev.* B **80** 155436
[97] Schülli T U, Stangl J, Zhong Z, Lechner R T, Sztucki M, Metzger T H and Bauer G 2003 *Phys. Rev. Lett.* **90** 066105

[98] Wiebach T, Schmidbauer M, Hanke M, Raidt H, Kohler R and Wawra H 2000 *Phys. Rev.* B **61** 5571
[99] Ratto F, Costantini G, Rastelli A, Schmidt O, Kern K and Rosei F 2006 *J. Exp. Nanosci.* **1** 279
[100] Spencer B J and Blanariu M 2005 *Phys. Rev. Lett.* **95** 206101
[101] Tsao J Y 1993 *Materials Fundamentals of Molecular Beam Epitaxy* (San Diego, CA: Academic)
[102] Denker U, Stoffel M and Schmidt O G 2003 *Phys. Rev. Lett.* **90** 196102
[103] Katsaros G, Costantini G, Stoffel M, Esteban R, Bittner A M, Rastelli A, Denker U, Schmidt O G and Kern K 2005 *Phys. Rev.* B **72** 195320
[104] Lang C, Cockayne D J H and Nguyen-Manh D 2005 *Phys. Rev.* B **72** 155328
[105] Kelires P C 2004 *J. Phys.: Condens. Matter* **16** S1485
[106] Gatti R, Uhlík F and Montalenti F 2008 *New J. Phys.* **10** 083039
[107] Tu Y and Tersoff J 2007 *Phys. Rev. Lett.* **98** 096103
[108] Persichetti L, Capasso A, Sgarlata A, Fanfoni M, Motta N and Balzarotti A 2012 *Self-Assembly of Nanostructures* ed S Bellucci (New York: Springer) p 201
[109] Persichetti L, Sgarlata A, Mattoni G, Fanfoni M and Balzarotti A 2012 *Phys. Rev.* B **85** 195314
[110] Persichetti L, Sgarlata A, Fanfoni M and Balzarotti A 2013 *J. Phys.: Condens. Matter* **25** 075802